CHAPTER 3

Energy Transfer to Phonons in Atom and Molecule Collisions with Surfaces

J.R. MANSON

Department of Physics and Astronomy
Clemson University
Clemson, SC 29634, *USA*

DOI: 10.1016/S1573-4331(08)00003-6

Handbook of Surface Science
Volume 3, edited by E. Hasselbrink and B.I. Lundqvist

Contents

Abstract

Experiments measuring the scattering of molecular beams from surfaces are capable of providing important information on the gas–surface interaction. However, such experiments are often carried out under conditions in which a substantial amount of the energy transfer is through excitations of phonons at the surface. This paper reviews theoretical methods of treating energy transfer to the surface from the limit of purely quantum mechanical elastic diffraction and single phonon transfer to the classical limit of large numbers of phonon excitations. In the multiphonon limit, theories of molecule–surface scattering are discussed which are classical in the translational and rotational degrees of freedom but quantum mechanical in the treatment of internal molecular vibrational modes. Through direct comparison with experiments it is shown that qualitative and quantitative explanations, as well as important physical information, can be obtained for many phenomena involving multiple phonon excitation observed in molecule–surface collisions. Examples are discussed that include both situations in which multiphonon excitation is the primary object of study and cases in which it is a secondary effect that must be accounted for. These examples include scattered angular distributions, translational energy-resolved measurements, rotational energy resolved spectra and internal vibrational mode excitation probabilities.

3.1. Introduction

This paper concerns the exchange of energy in the collision of molecules with a surface. In particular, it is intended as a useful review for describing energy transfer in experiments in which a well-defined molecular beam is directed towards a surface and the final states of the molecules eventually leaving the surface are measured in a detector. Typical experiments are carried out under ultra-high vacuum conditions with projectiles ranging from the smallest possible masses such as H_2 molecules or He atoms to large mass gases, and energies are usually in the thermal to hypersonic range which corresponds to translational energies from a few meV to several eV. A collision with the surface can lead to a variety of different outcomes, for example the molecules leaving the surface may be directly scattered, they can be briefly trapped at the surface, or may be adsorbed for longer times before eventually desorbing. In all cases an important channel for exchange of energy is phonon annihilation or creation, and in most cases this is by far the dominant mechanism for energy transfer although excitation of electron–hole pairs or other elementary electronic excitations may play a role for high energies and larger mass gas particles.

One of the earliest experiments to attempt to characterize the nature of atom surface collisions was that of Roberts who measured energy transfer between rare gases and a tungsten surface (Roberts, 1930). These experiments stimulated theoretical calculations by Mott and Jackson using the methods of quantum mechanics which were being developed at the time (Jackson and Mott, 1932; Jackson, 1932). Their calculations were the first to describe the energy transfer in surface scattering by what is now known as a single-phonon distorted wave Born approximation. Also during the early years of quantum mechanics Stern and co-workers started a long series of experiments, primarily scattering of He beams from LiF(001) surfaces, in which the apparent motivating objective was to confirm the de Broglie matter wave hypothesis through observation of diffraction peaks (Frisch, 1979; Stern, 1920a, 1920b, 1926; Knauer and Stern, 1929; Estermann and Stern, 1930; Estermann et al., 1931). This seminal work prompted a series of publications by Lennard-Jones and his students that pointed out the importance of trapping in the physisorption potential well and the importance of energy transfer to the phonons (Lennard-Jones and Devonshire, 1936a, 1936b, 1936c, 1936d, 1937a, 1937b, 1936b). Their calculations were also done in the distorted wave Born approximation, and they even investigated multiple phonon transfers, although we know today that the multiple phonon excitations they calculated (Strachan, 1935) are not the dominant contribution to multiple phonon energy exchange (Manson and Tompkins, 1977).

With the advent in the 1960s and 1970s of improved ultra-high vacuum techniques, together with the development of highly mono-energetic molecular jet beams, there was a renewed interest in gas–surface experiments. This led to measurements that were capable of detecting single surface phonon creations and annihilations and the first measurements of surface phonon dispersion relations (Brusdeylins et al., 1980, 1981). These experiments have developed to the point that today He atom scattering from surfaces is a standard method of obtaining surface sensitive information. The scattering of many other atomic and molecular particles is used to obtain information on both the surfaces, the molecule–surface interaction potential, and on surface chemical reactions.

In all such experiments, energy transfer to the phonons is important. In many cases, a significant portion of the incident translational energy can be lost upon collision, for example in the case of NO or N_2 scattering from typical metal surfaces, a beam with incident energy of order 1 eV can lose 25–75% of its energy into phonons, which essentially means transferring heat to the surface. Such large energy transfers will have a substantial effect on other processes such as adsorption and excitation of internal molecular modes and thus must be understood. Even in the case of He atom scattering at thermal energies, where the dominant inelastic processes tend to be single phonon excitation of Rayleigh and other surface modes, there is a background in the energy-resolved scattering spectrum that is in large part due to multiphonon events. Identifying and subtracting this background from the single phonon contributions is an essential problem because under certain circumstances the multiphonon background can produce peaks in the scattering spectra that resemble single phonon features (Celli et al., 1991). However, background subtraction is far from the only reason for needing an understanding of multiphonon events. Important features of the molecule–surface interaction potential are revealed in the behavior of multiphonon spectra and, since the study of multiple phonon events ranges from small to large quantum numbers of excitation, it provides an interesting example of the transition from purely quantum phenomena to classical physics at large quantum numbers.

Much of the study of phonon excitation in molecule–surface collisions has been treated in earlier reviews, a partial list of which is given in Hulpke (1992), Bortolani and Levi (1986), Toennies (1991), Rettner and Ashfold (1991), Barker and Auerbach (1984), Celli (1984), Toennies (1987), Scoles (1988) Campargue (2001) Benedek and Toennies (1994), Manson (1994), Gumhalter (2001). The organization of this paper is as follows. The next section (Section 3.2) presents a simple and elegant elementary model for describing scattering events in which large numbers of phonons are transferred. This model serves as a basis for understanding and developing a variety of theoretical approaches that have been used for multiphonon scattering from surfaces by atoms and molecules. A brief description of the quantities actually measured in experiments and how they relate to the calculated scattering probabilities is in Section 3.3. In Section 3.4 a general approach to the theory of surface scattering that can be applied to multiple phonon energy transfers is developed. This theory begins with atomic projectiles and then extends the treatment to include the internal degrees of freedom of molecules. The theoretical approach is illustrated and discussed through comparisons with several different types of experimental scattering intensity measurements in Section 3.5. Further discussion and some conclusions are presented in Section 3.6.

3.2. Basic model for multiphonon excitation

Although it will be seen in the sections below that the multiphonon contributions to scattering spectra can be manifest in many different forms, the basic aspects of multiphonon energy transfer in many molecule–surface scattering experiments can often be understood and analyzed within the framework of a classical model for energy transfer between an atomic projectile and a target consisting of discrete atoms. This model is perhaps best expressed mathematically in terms of the transition rate $w(\mathbf{p}_f, \mathbf{p}_i)$ which is the probability

per unit time that a particle initially in a state of momentum $\mathbf{p}_i$ will make a transition to the final state $\mathbf{p}_f$. This is the same transition rate that is used as the fundamental starting point in the quantum mechanical description of scattering theory (Rodberg and Thaler, 1967) and it provides a convenient description that is independent of any effects imposed by the constraints of the particular experiment used to measure the scattering. The ways in which actual experimentally measured quantities can be determined from the transition rate $w(\mathbf{p}_f, \mathbf{p}_i)$ is discussed below in Section 3.3.

The basic transition rate, which can be calculated from purely classical mechanics, for an atomic projectile of mass m colliding with a target of atomic scattering centers with mass M_C and whose initial velocity distribution is determined by the equilibrium condition of equipartition of energy is

$$w(\mathbf{p}_f, \mathbf{p}_i) = \frac{1}{\hbar}|\tau_{fi}|^2\left[\frac{\pi}{k_B T_S \Delta E_0^T}\right]^{\frac{1}{2}} \exp\left\{-\frac{(E_f^T - E_i^T + \Delta E_0^T)^2}{4k_B T_S \Delta E_0^T}\right\}, \tag{3.1}$$

where the translational energy is $E_f^T = \mathbf{p}_f^2/2m$, T_S is the surface temperature, k_B is Boltzmann's constant, and the recoil energy is given by $\Delta E_0^T = (\mathbf{p}_f - \mathbf{p}_i)^2/2M_C$. $|\tau_{fi}|^2$ is a form factor that depends on the interaction potential between projectile and target atoms, for example, it is a constant for hard sphere collisions. The quantity $\hbar$ is a constant having dimensions of action and the first principles quantum mechanical derivation given below in Section 3.4 shows that this is properly identified to be Planck's constant divided by 2π.

Equation (3.1) is quite old, having been used to describe multiphonon scattering in neutron scattering (Sjölander, 1959) and ion scattering (Micha, 1981). It actually gives a very good quantitative description of the single collision peak observed in certain low energy ion scattering experiments (Muis and Manson, 1996; Powers et al., 2004). At first glance, Eq. (3.1) appears to be a Gaussian-like function of the energy difference $E_f^T - E_i^T$ but in actual practice under many initial conditions it can be highly skewed and appear quite different from Gaussian-like behavior. For example, in the limit of very small incident energy Eq. (3.1) goes over to exponential behavior in the final energy

$$w(\mathbf{p}_f, \mathbf{p}_i) = \frac{1}{\hbar}|\tau_{fi}|^2\left[\frac{\pi}{k_B T_S \mu E_f^T}\right]^{\frac{1}{2}} \exp\left\{-\frac{E_f^T(1+\mu)^2}{4k_B T_S \mu}\right\}, \tag{3.2}$$

where the mass ratio is $\mu = m/M_C$.

Under many initial conditions, Eq. (3.1) does look Gaussian like. For example, for the incident energy E_i^T large compared to $k_B T_S$ and $\mu < 1$ it has only a single peak when plotted as a function of final energy E_f^T at fixed incident and final angles. The position of the peak, or the most probable final energy, lies very nearly at the zero of the argument of the exponential which is given by the Baule condition $\overline{E_f^T} = f(\theta)E_i^T$ in which θ is the total scattering angle (the angle between $\mathbf{p}_f$ and $\mathbf{p}_i$) and $f(\theta)$ is given by

$$f(\theta) = \left(\frac{\sqrt{1-\mu^2\sin^2\theta} + \mu\cos\theta}{1+\mu}\right)^2. \tag{3.3}$$

The width of this peak, expressed as the mean-square deviation from the most probable energy is approximately

$$\left\langle (\Delta E^T)^2 \right\rangle \approx 2g(\theta) E_i^T k_B T_S, \tag{3.4}$$

where

$$g(\theta) = \frac{g_{TA}(\theta)}{1 + \mu - \frac{\mu \cos\theta}{\sqrt{f(\theta)}}}, \tag{3.5}$$

with

$$g_{TA}(\theta) = \mu\left(1 + f(\theta) - 2\sqrt{f(\theta)}\cos\theta\right). \tag{3.6}$$

The function $g_{TA}(\theta)$ is the approximation to $g(\theta)$ that is obtained in the so-called trajectory approximation (Burke et al., 1991; DiRubio et al., 1994). The intensity at the position of the most probable final energy peak is dictated by the prefactor, or envelope function, which goes as

$$I_{MAX} \propto \frac{1}{(k_B T_S \Delta E_0^T)^{1/2}} \approx \frac{1}{(k_B T_S g_{TA}(\theta) E_i^T)^{1/2}}. \tag{3.7}$$

The fact that the width increases with the square root of temperature and energy while the maximum intensity decreases with the same square root behavior is indicative of the unitarity property of the differential reflection coefficient of Eq. (3.1), i.e., it is normalizable which indicates that the number of scattered particles equals the number incident. Eqs. (3.3) through (3.6) are recognized as the familiar expressions associated with the properties of collisions of two rigid spheres and generally attributed to the work of Baule dating from the early 1900s (Baule, 1914; Goodman, 1974). The general behavior of Eq. (3.1) can become more complex, for example if $\mu > 1$ it can exhibit double peaks or no well-defined peaks at all depending on the scattering angles.

An important, and perhaps somewhat surprising property of Eq. (3.1) is that it depends in no way on the vibrational properties of the target, in fact it will be shown below that it depends only on a distribution of velocities in the target that obeys the equilibrium property of equipartition of energy, examples being thermal vibrations in solids or the distribution of speeds in a gas. This is the same as saying that even though Eq. (3.1) describes energy transfer with the vibrational modes it contains no information about the phonons or any other elementary excitations, such as electron–hole pairs, that may have been created. It describes a collision event in which the projectile atom collides with a target atom, the target recoils, but the projectile then leaves the scene of the collision before the recoiling target atom has an opportunity to create vibrations or other excitations in the target. The recoiling atom eventually does create a cloud of multiple phonon excitations, but by this time the original projectile is far away and carries no detailed information about the nature of the excitations created and destroyed.

In spite of its simplicity, and the paucity of information about the properties of the target contained in Eq. (3.1), it and its many related forms are very useful in describing multi-phonon energy transfer observed in particle–surface scattering experiments. Specifically, Eq. (3.1) and its properties described in Eqs. (3.3) through (3.7) have been shown to explain the temperature and energy dependence of single scattering events in low energy ion

scattering, specifically for Na^+ and K^+ scattering from Cu(100) (Muis and Manson, 1996; Powers et al., 2004). It has also been used to describe the energy resolved scattering spectra observed in experiments of rare gases scattering from metal surfaces (Muis and Manson, 1997; Dai and Manson, 2003).

A straightforward way of deriving Eq. (3.1) above is to recognize that in a collision of an atomic projectile with a discrete target core the transition rate will depend on the essential conditions of conservation of momentum and energy between target and projectile, i.e., the transition rate will be of the form

$$w(\mathbf{p}_f, \mathbf{p}_i) \propto \left\langle \sum_{\mathbf{k}_f} F\delta\big(E_f^T + \varepsilon_f^T - E_i^T - \varepsilon_i^T\big)\delta(\mathbf{p}_f + \mathbf{k}_f - \mathbf{p}_i - \mathbf{k}_i) \right\rangle \tag{3.8}$$

where $\mathbf{k}_i$ and $\mathbf{k}_f$ are the translational momentum of the target atom before and after the collision, respectively, ε_i^T and ε_i^T are the corresponding target atom energies, and F is a function depending on all final and initial momenta which will be related below to the scattering form factor $|\tau_{fi}|^2$. Because the initial and final states of the target particles are not measured in a typical experiment, the transition rate must be averaged over all initial states of the many-body target as signified by the symbol $\langle\ \rangle$ and also must be summed or integrated over all final momenta of the target. The summation over final target momenta is trivially carried out leading to

$$w(\mathbf{p}_f, \mathbf{p}_i) \propto \left\langle F\delta\left(E_f^T - E_i^T + \frac{\mathbf{p}^2}{2M_C} - \frac{\mathbf{k}_i \cdot \mathbf{p}}{M_C} \right) \right\rangle, \tag{3.9}$$

where $\mathbf{p} = \mathbf{p}_f - \mathbf{p}_i$ is the momentum scattering vector. Next, the energy δ-function is represented by its Fourier transform over time t, and additionally making the assumption that F is independent of the initial target momentum, the transition rate becomes

$$w(\mathbf{p}_f, \mathbf{p}_i) \propto \frac{F(\mathbf{p}_f, \mathbf{p}_i)}{2\pi\hbar} \int_{-\infty}^{+\infty} \mathrm{d}t\, e^{-i(E_f^T - E_i^T + \frac{\mathbf{p}^2}{2M_C})t/\hbar} \left\langle e^{-i\frac{\mathbf{k}_i \cdot \mathbf{p}}{M_C}\frac{t}{\hbar}} \right\rangle, \tag{3.10}$$

where as mentioned above $\hbar$ is a constant having dimensions of mechanical action. (In a quantum mechanical treatment, $\hbar$ becomes Planck's constant divided by 2π as is indicated in the treatments of Section 3.4 below (Sjölander, 1959; Brako and Newns, 1982; Brako, 1982; Manson, 1991).)

The average over initial target states appearing in Eq. (3.10) is readily carried out assuming three dimensional isotropy of initial motion and using a Maxwell–Boltzmann distribution of momenta.

$$\left\langle \exp\left\{ -i\frac{\mathbf{k}_i \cdot \mathbf{p}}{M_C}\frac{t}{\hbar} \right\} \right\rangle = \exp\left\{ -\frac{\mathbf{p}^2}{2M_C} k_B T_S \frac{t^2}{\hbar^2} \right\} = \exp\left\{ -\Delta E_0^T k_B T_S \frac{t^2}{\hbar^2} \right\}. \tag{3.11}$$

Now, when the result of Eq. (3.11) is used in Eq. (3.10), the Fourier transform is a simple Gaussian integral and the result is precisely the discrete target transition rate of Eq. (3.1), after making the identification $F(\mathbf{p}_f, \mathbf{p}_i) \propto |\tau_{fi}|^2$ for the form factor. This derivation of Eq. (3.1) is not only straightforward and direct, it also points out very clearly all assumptions and approximations which are used in its derivation. In particular it is derived from purely classical physics, its form is dictated by the energy and momentum conservation

laws, and the statistical mechanics depends only on the equilibrium equipartition of initial momenta in the target.

In the sections below, the theoretical treatment of inelastic molecule–surface scattering with energy transfer to the phonons of the target will be reviewed. This will cover the range from purely quantum mechanical processes with only a single phonon excited to the classical limit of many phonons as manifest in the example equation of Eq. (3.1). In the process a series of expressions related to Eq. (3.1) will be developed, all of which have shown applicability to explaining molecule surface scattering experiments. Eq. (3.1), which is the limiting case for a collection of discrete target atoms, will be extended to scattering from smooth surface barriers and to include excitation of internal rotational and vibrational degrees of freedom of the projectile.

3.3. Experimentally measured quantities

The transition rate for atomic scattering $w(\mathbf{p}_f, \mathbf{p}_i)$ depends only on the final and initial translational momenta, while for molecular scattering it will depend also on the internal modes, i.e., the transition rate becomes $w(\mathbf{p}_f, \mathbf{l}_f, \alpha_{jf}; \mathbf{p}_i, \mathbf{l}_i, \alpha_{ji})$ where $\mathbf{l}_f$ or $\mathbf{l}_i$ are the angular momenta for the final and initial states, respectively, and α_{jf} or α_{ji} are the excitation quantum numbers for the jth internal vibrational mode in the final or initial state. The transition rate is a useful quantity on which to base the calculations because it gives the probability per unit time for the transition between two well defined molecular states and is independent of the experimental configuration. Quantities which are actually measured in experiments, such a cross sections or differential reflection coefficients, are proportional to $w(\mathbf{p}_f, \mathbf{l}_f, \alpha_{jf}; \mathbf{p}_i, \mathbf{l}_i, \alpha_{ji})$ with the proportionality given by an appropriate Jacobian density of states that depends on the nature of the experimental apparatus. Since experimental configurations, and detector devices, can vary considerably it is worthwhile to give a brief description of the relationship between the transition rate and quantities that are measured.

In an idealized surface scattering experiment what is often measured is the differential reflection coefficient, essentially a differential cross section per unit surface area, given by the transition rate normalized to the incident beam flux with the phase space differential volume element converted to spherical coordinates

$$\frac{\mathrm{d}^3 R(\mathbf{p}_f, \mathbf{l}_f, \alpha_{jf}; \mathbf{p}_i, \mathbf{l}_i, \alpha_{ji})}{\mathrm{d}E_f^T \, \mathrm{d}\Omega_f} = \frac{L^4}{(2\pi\hbar)^3} \frac{m^2 |\mathbf{p}_f|}{p_{iz}} w(\mathbf{p}_f, \mathbf{l}_f, \alpha_{jf}; \mathbf{p}_i, \mathbf{l}_i, \alpha_{ji}), \quad (3.12)$$

where L is a quantization length and $p_{iz} = p_i \cos(\theta_i)$ is the incident perpendicular momentum and this appears because it is proportional to the incident particle flux crossing a plane parallel to the surface. The factor of p_f arises from expressing the element of phase space volume in spherical coordinates $\mathrm{d}^3 p_f = p_f^2 \, \mathrm{d}p_f \, \mathrm{d}\Omega_f = m p_f \, \mathrm{d}E_f^T \, \mathrm{d}\Omega_f$. Equation (3.12) gives the probability per unit final translational energy E_f^T and per unit final solid angle Ω_f that a particle initially prepared in a state denoted by quantum numbers i will make a transition to the final state denoted by quantum numbers f.

Equation (3.12) is a good representation of what is actually measured by a large number of atomic and molecular surface scattering experiments. It describes an experiment in

which all particles scattered from the surface in a particular angular direction can enter the detector, and in practical terms this means that the acceptance angle of the detector is large enough to "see" the entire spot on the surface illuminated by the incident beam. Also, in practical terms, the differential energy element dE_f^T is the smallest element of energy resolvable by the detection apparatus and $d\Omega_f$ is the solid angle subtended by the detector aperture measured relative to the sample.

The type of detector used in the experiment can introduce additional corrections to the differential reflection coefficient of Eq. (3.12). In many experiments, the final molecule is detected as it passes through a short detection length and the overall probability of detection is small. In this case, the detection probability is proportional to the time spent traversing the detector length, which is inversely proportional to the translational speed. Thus for this type of detector, often referred to as a density detector, the differential reflection coefficient must be divided by a factor of p_f to account for the detector correction. As examples of other types of detectors, a stagnation detector for atomic scattering requires no correction to Eq. (3.12) while for ion scattering a typical detector is an electrostatic analyzer which requires a correction of $1/p_f^2$.

Another variant of detector correction occurs in experiments utilizing a very large distance between the sample and the detector, such as very long time-of-flight arm used to obtain high translational energy resolution (Brusdeylins et al., 1980, 1981). In such cases the acceptance angle of the detector may be reduced to the point where the detector "sees" only a small portion of the illuminated spot on the sample. In this case, the factor $1/\cos(\theta_i)$ associated with the factor $1/p_{iz}$ appearing on the right hand side of Eq. (3.12) must be replaced by $1/\cos(\theta_f)$. The reason for this is that in Eq. (3.12) the factor $1/\cos(\theta_i)$ accounts for the increase in total area of the spot on the sample surface that is illuminated by the incident beam. However, if the detector does not accept the intensity coming from the whole spot but "sees" only a small portion of this spot then the total area of illuminated surface seen by the detector is dictated by the final scattering angle through a factor of $1/\cos(\theta_f)$. Clearly, these two possibilities represent two extremes, and there are many experimental situations in which the illuminated beam spot and the area subtended by the detector are comparable in size. In such situations the geometrical correction factors can get quite complicated.

The above remarks on detector corrections represent only a small and idealized sampling of situations that can arise in actual experimental configurations. However, determining the corrections that must be used in each situation can be quite important in comparing theoretical calculations with measurements. For example, in measurements of translational energy-resolved spectra the intensity of scattered particles is plotted as a function of final translational energy. Narrow single surface phonon peaks in such a plot will not be appreciably shifted by a detector correction such as a factor of $1/p_f$ but their relative intensities will be affected. On the other hand, a broad multiphonon background peak will have both its intensity altered and peak position shifted by such a correction, and at low energies such shifts can amount to a substantial fraction of the incident beam energy. Thus, it becomes important to take into account detector corrections in comparing calculations with data.

3.4. Surface scattering theory

3.4.1. General treatment

A starting point for describing molecular scattering from a many-body target is the quantum mechanical state-to-state transition rate for a molecular projectile prepared in a well-defined incident state denoted by the set of quantum numbers $\{\mathbf{p}_i, \mathbf{l}_i, \alpha_{ji}\}$ making a transition to a final state denoted by $\{\mathbf{p}_f, \mathbf{l}_f, \alpha_{jf}\}$ This is given by the generalized Fermi golden rule (Rodberg and Thaler, 1967)

$$w(\mathbf{p}_f, \mathbf{l}_f, \alpha_{jf}; \mathbf{p}_i, \mathbf{l}_i, \alpha_{ji}) = \left\langle \frac{2\pi}{\hbar} \sum_{\{n_f\}} |\mathcal{T}_{fi}|^2 \delta(\mathcal{E}_f - \mathcal{E}_i) \right\rangle, \tag{3.13}$$

where the average over initial translational and rotational states of the target crystal is denoted by $\langle\ \rangle$ and the sum is over all unmeasured final states $\{n_f\}$ of the crystal which can scatter a projectile into its specified final state. The energies $\mathcal{E}_i$ and $\mathcal{E}_f$ refer to the total energy of the system of projectile molecule plus the crystal before and after collision, respectively. The $\mathcal{T}_{fi}$ are the matrix elements of the transition operator $\mathcal{T}$ taken with respect to unperturbed initial and final states of the system. The transition rate is the fundamental quantity for describing a scattering process, because all measurable quantities in a scattering experiment can be calculated from it.

In the semiclassical limit, the transition rate can be expressed as the Fourier transform over all times of a generalized time-dependent correlation function. In this same level of approximation, it is useful to assume the decoupling approximation which in this instance means that the elastic part of the interaction potential is assumed to commute with the inelastic part, and the transition rate is expressed as (Bortolani and Levi, 1986; Manson et al., 1994)

$$\begin{aligned} &w(\mathbf{p}_f, \mathbf{l}_f, \alpha_{jf}, \mathbf{p}_i, \mathbf{l}_i, \alpha_{ji}) \\ &\quad = \frac{1}{\hbar^2} |\tau_{fi}|^2 \int_{-\infty}^{\infty} e^{-i(E_f - E_i)t/\hbar} \exp\{-2\mathcal{W}\} \exp\big\{\mathcal{Q}(t)\big\}\, \mathrm{d}t, \end{aligned} \tag{3.14}$$

where $\exp\{-2\mathcal{W}\}$ is a generalized Debye–Waller factor and $\mathcal{Q}(t)$ is a generalized time-dependent correlation function. $|\tau_{fi}|^2$ is the scattering form factor which becomes the square modulus of the off-energy-shell transition matrix of the elastic part of the interaction potential.

There can be several mechanisms for energy transfer in the collision process, such as phonons, rotational excitations, and internal mode excitations, each of which is considered here. If each of these processes is considered as independent, then the transition rate can be written in this separability limit as

$$\begin{aligned} &w(\mathbf{p}_f, \mathbf{l}_f, \alpha_{jf}, \mathbf{p}_i, \mathbf{l}_i, \alpha_{ji}) \\ &\quad = \frac{1}{\hbar^2} |\tau_{fi}|^2 \int_{-\infty}^{\infty} e^{-i(E_f^T - E_i^T + E_f^R - E_i^R + E_f^V - E_i^V)t/\hbar} \\ &\qquad \times K_T(t, T_S) K_R(t, T_S) K_V(t, T_B)\, \mathrm{d}t, \end{aligned} \tag{3.15}$$

where as in Eq. (3.1) $E^T_{f,i}$ is the translational energy of the final (f) or initial (i) projectile state, $E^R_{f,i}$ is the corresponding rotational energy of the projectile, and $E^V_{f,i}$ is the energy of the projectile's internal vibrational state. $K_T(t, T_S)$ is the scattering kernel for translational motion and phonon excitation, $K_R(t, T_S)$ is the scattering kernel for rotational excitation, and $K_V(t, T_B)$ is the kernel for internal vibrational mode excitation. Equation (3.15) is self consistent in the following sense: although each of the three energy exchange mechanisms is treated as being independent, each operates taking into consideration the energy losses or gains caused by the other mechanisms.

Starting from Eq. (3.15), the problem now becomes one of choosing models for the scattering kernels for each of the energy exchange processes and this is done in the following. In the next subsection energy transfers between the translational energy of a simple atomic projectile and the phonon modes are developed. Section 3.4.3 gives a discussion of the molecular rotational degrees of freedom by treating a rigid rotating molecule colliding with the surface. In Section 3.4.4 the full problem of a molecule with both rotational and vibrational degrees of freedom is discussed.

3.4.2. Atom–surface scattering

In order to begin with the phonon modes it is convenient to temporarily ignore the internal degrees of freedom of the molecule and consider the problem of a pseudo-atomic projectile interacting with the surface. For the interaction with phonons, an extension of the semiclassical model originally introduced by Brako and Newns for inelastic scattering of ions and atoms from smooth surfaces is a useful approach (Bortolani and Levi, 1986; Brako and Newns, 1982; Brako, 1982). They showed that in the semiclassical limit the phonon scattering kernel can be expressed in terms of a general exponentiated correlation function $Q_T(\mathbf{R}, t)$, where $\mathbf{R}$ is the position vector parallel to the surface, as

$$K_T(t, T_S) = \int_{-\infty}^{\infty} \mathrm{d}\mathbf{R}\, e^{i\mathbf{K}\cdot\mathbf{R}} e^{-2W_T(\mathbf{p}_f, \mathbf{p}_i)} e^{Q_T(\mathbf{R}, t)}, \tag{3.16}$$

where $2W_T(\mathbf{p}_f, \mathbf{p}_i) = Q_T(\mathbf{R} = 0, t = 0)$ is the contribution to the total Debye–Waller factor due to phonon exchange.

If the semiclassical limit is now extended to the limit of rapid collisions in which the semiclassical force exerted on the scattering particle can be replaced by the momentum impulse, then the correlation function simplifies to the time dependent displacement correlation function

$$Q_T(\mathbf{R}, t) = \big\langle \mathbf{p}\cdot\mathbf{u}(0, 0)\mathbf{p}\cdot\mathbf{u}(\mathbf{R}, t)\big\rangle \big/ \hbar^2, \tag{3.17}$$

where $\mathbf{u}(\mathbf{R}, t)$ is the phonon displacement at the position $\mathbf{R}$ on the surface. The argument of the Debye–Waller factor is given by the standard form, which for T_S greater than the Debye temperature Θ_D is

$$W_T(\mathbf{p}_f, \mathbf{p}_i) = \big\langle \big(\mathbf{p}\cdot\mathbf{u}(0, 0)\big)^2 \big\rangle \big/ \hbar^2 = \frac{3p^2 T_S}{2M_C k_B \Theta_D^2}. \tag{3.18}$$

In addition to the straight-forward choice of Eq. (3.17) there are other possibilities for the correlation function $Q_T(\mathbf{R}, t)$ that have been proposed. One choice that has been

very successful in explaining multiphonon transfers in He atom scattering from surfaces is the exponentiated Born approximation which in its simplest formulation consists of replacing the impulse $\mathbf{p}$ appearing in Eq. (3.17) with the distorted wave Born approximation matrix element of the first derivative of the interaction potential with respect to the phonon displacement vectors (Burke et al., 1993; Gumhalter et al., 1994; Gumhalter and Langreth, 1999).

Equation (3.16) provides a standard and very convenient method for developing the scattering transition rate into an ordered series in numbers of phonons transferred in the collision process. This is by simply expanding the exponentiated correlation function in powers of its argument $Q_T(\mathbf{R}, t)$. The zero order term gives the elastic scattering contribution and results in

$$w(\mathbf{p}_f, \mathbf{p}_i) = \frac{2\pi}{\hbar} \sum_{\mathbf{G}} |\tau_{\mathbf{p}_f, \mathbf{p}_i}|^2 e^{-2W(\mathbf{p})} \delta_{\mathbf{P}, \hbar\mathbf{G}} \delta\big(E_f^T - E_i^T\big), \tag{3.19}$$

where $\mathbf{P}$ is the parallel component of the momentum transfer $\mathbf{p}$, $\mathbf{G}$ is a reciprocal lattice vector of the surface and $\tau_{\mathbf{p}_f, \mathbf{p}_i}$ is the transition matrix element of the static elastic interaction potential taken between final state $\mathbf{p}_f$ and initial state $\mathbf{p}_i$. Eq. (3.19) is in fact the exact quantum mechanical expression for diffraction from a periodic surface and it is seen that scattered intensity is observed only if both energy is conserved and if momentum parallel to the surface is conserved modulo a surface reciprocal lattice vector multiplied by $\hbar$.

To obtain the single phonon contribution $\exp\{Q_T(\mathbf{R}, t)\}$ is expanded to first order which leads to the following approximation to the expression for the transition rate

$$w(\mathbf{p}_f, \mathbf{p}_i) = \frac{2\pi}{\hbar} \sum_{\mathbf{G}} |\tau_{\mathbf{p}_f, \mathbf{p}_i}|^2 e^{-2W(\mathbf{p})} \big[n(\omega) + 1\big] \mathbf{p} \cdot \underline{\underline{\boldsymbol{\rho}(\mathbf{P} + \hbar\mathbf{G}, \omega)}} \cdot \mathbf{p} \tag{3.20}$$

where $n(\omega)$ is the Bose–Einstein distribution function for a phonon of frequency ω and $\underline{\underline{\boldsymbol{\rho}(\mathbf{P} + \hbar\mathbf{G}, \omega)}}$ is the phonon spectral density tensor, i.e., the function that completely specifies the phonon spectrum of the surface as a function of momentum and frequency (Maradudin et al., 1963). Equation (3.19) is the expression for single phonon creation. The expression for single phonon annihilation is obtained by replacing $n(\omega)+1$ by $n(\omega)$. Equation (3.19) is a simple version of one of many approximations proposed for treating single phonon transfers in atom–surface scattering that have proven to be very useful in describing aspects of single phonon He atom scattering (Hulpke, 1992; Bortolani and Levi, 1986; Celli, 1984; Gumhalter, 2001; Hofmann et al., 1994, 1997). A form of the well-known distorted wave Born approximation is obtained if the transition matrix $\tau_{\mathbf{p}_f, \mathbf{p}_i}$ is replaced by a matrix element of the elastic term of the scattering potential taken with respect to states $\mathbf{p}_f$ and $\mathbf{p}_i$ corresponding to energies that differ by the phonon energy $\hbar\omega$.

The classical limit of multiple phonon exchange is obtained from Eqs. (3.17) and (3.16) by making an expansion of the correlation function $Q_T(\mathbf{R}, t)$ over small times and small position vectors around the point of collision, leading to

$$\begin{aligned} \big\langle \mathbf{p} \cdot \mathbf{u}(0,0) \mathbf{p} \cdot \mathbf{u}(\mathbf{R}, t) \big\rangle \big/ \hbar^2 = {} & 2W_T(\mathbf{p}_f, \mathbf{p}_i) - \frac{i}{\hbar} t \Delta E_0^T \\ & - \frac{t^2}{\hbar^2} \Delta E_0^T k_B T_S - \frac{\Delta E_0^T k_B T_S R^2}{2\hbar^2 v_R^2}, \end{aligned} \tag{3.21}$$

where v_R is a weighted average over phonon velocities parallel to the surface (Brako and Newns, 1982; Brako, 1982).

If phonons are the only mechanism for energy transfer, such as is often the case in atom scattering, then the scattering kernel developed in Eqs. (3.16)–(3.21) leads to a transition rate that is Gaussian-like in both the translational energy transfer $E_f^T - E_i^T$ and the parallel component $\mathbf{P}$ of the momentum transfer (Brako and Newns, 1982; Brako, 1982; Manson, 1991; Meyer and Levine, 1984)

$$w(\mathbf{p}_f, \mathbf{p}_i) = \frac{2\hbar v_R^2}{S_{u.c.}} |\tau_{fi}|^2 \left(\frac{\pi}{k_B T_S \Delta E_0} \right)^{3/2} \exp\left\{ - \frac{(E_f^T - E_i^T + \Delta E_0)^2 + 2v_R^2 \mathbf{P}^2}{4 k_B T_S \Delta E_0} \right\}. \tag{3.22}$$

This is the smooth surface scattering model for classical multiphonon transfers in an atom–surface collision. It takes into account the broken symmetry in the perpendicular direction caused by the presence of the surface, i.e., for every phonon exchanged only momentum parallel to the surface is conserved. The perpendicular momentum exchange is not conserved as a consequence of the broken symmetry in that direction. The Debye–Waller factors, normally present in quantum mechanical theory, have disappeared because they were canceled by the first term in Eq. (3.21) leaving the Gaussian-like behavior with an envelope factor that varies as the negative $3/2$ power of the recoil energy and surface temperature.

There are also other classical expressions for describing classical multiphonon exchange in atomic collisions. If the surface is regarded as a collection of isolated scattering centers in thermodynamic equilibrium, then the scattering kernel in the classical limit becomes simpler than Eq. (3.21):

$$K_T(t, T_S) = \exp\left\{ -\frac{i}{\hbar} t \Delta E_0^T - \frac{t^2}{\hbar^2} \Delta E_0^T k_B T_S \right\}, \tag{3.23}$$

which leads to the expression of Eq. (3.1) described above in Section 3.2.

The smooth surface model of Eq. (3.22) differs from the discrete model of Eq. (3.1) in that it contains the additional Gaussian-like function of the parallel momentum transfer $\mathbf{P}$ and the envelope function (i.e., the prefactor) varies as the $-3/2$ power of $T_S \Delta E_0^T$ rather than the $-1/2$ power.

The physical difference between the two expressions of Eqs. (3.22) and (3.1) is the corrugation of the surface. Equation (3.22) describes a surface that is smooth except for the vibrational corrugations caused by the time dependent motions of the underlying atoms, while Eq. (3.1) describes a surface that is highly corrugated, so highly corrugated that each scattering center is distinct. Other models for the classical multiphonon limit have been proposed for surfaces that are corrugated in a manner intermediate between these two extreme limits (Manson, 1998). These intermediate models all have the common feature of Gaussian-like behavior in energy transfer, and in addition show that the mean square corrugation of the surface can be directly related to the temperature and recoil energy dependence of the envelope factor.

It is of interest to compare expressions of the type represented by Eqs. (3.22) and (3.1) to the results obtained by carrying out quantum mechanical perturbation theory to high orders in numbers of phonons transferred. The lowest order, single-phonon transfer term in perturbation theory is, for example, given by the distorted wave Born approximation of

Eq. (3.20) but in general each term in the perturbation series contributes to all orders of numbers of phonons excited. However, in atom–surface scattering, the dominant contributions to multiphonon transfer come from higher order terms in the perturbation series. For example, the double phonon contribution arising from the first order perturbation theory term is negligible compared to the double phonon contribution arising in second-order perturbation theory (Manson and Tompkins, 1977; Armand and Manson, 1984). It can readily be shown that expressions of the type of Eqs. (3.22) and (3.1) can be related to summations to all orders of the perturbation series in which only the smallest numbers of phonon excitations are retained in each term (Manson, 1994). The perturbation series can be calculated term by term, and such calculations have sometimes been useful in the study of multiphonon excitation in atom–surface scattering (Armand and Manson, 1984; Armand et al., 1986), but this approach rapidly leads to lengthy and cumbersome calculations for large numbers of phonons excited.

3.4.3. Rigid molecular rotator

The next task is to develop a scattering kernel for the rotational motion of the molecular projectile. In order to be consistent with the smooth surface model of Eq. (3.22) for the translational motion, a model is developed that preserves the correct angular momentum conservation for a rotating molecule interacting with a smooth surface, i.e., angular momentum will be conserved in the direction perpendicular to the surface but not in the directions parallel to the surface. Starting from Eq. (3.13) in the semiclassical limit, but with the proper angular momentum conservation for a smooth surface, the scattering kernel for rotational motion is (Dai and Manson, 2002)

$$K_R(t, T_S) = \int_{-\infty}^{\infty} \mathrm{d}\theta_z \, e^{i l_z \theta_z/\hbar} e^{-2W_R(\mathbf{l}_f, \mathbf{l}_i)} e^{Q_R(\theta_z, t)}, \tag{3.24}$$

where $Q_R(\theta_z, t)$ is a generalized rotational correlation function and the rotational contribution to the Debye–Waller factor is $2W_R(\mathbf{l}_f, \mathbf{l}_i) = Q_R(\theta_z = 0, t = 0)$. In the limit of a quick collision, where the angular forces are given by the angular impulse, the correlation function becomes a correlation function of the angular displacement $\boldsymbol{\Theta}(\theta_z, t)$:

$$Q_R(\theta_z, t) = \left\langle \mathbf{l} \cdot \boldsymbol{\Theta}(0, 0) \mathbf{l} \cdot \boldsymbol{\Theta}(\theta_z, t) \right\rangle \big/ \hbar^2, \tag{3.25}$$

where $\mathbf{l} = \mathbf{l}_f - \mathbf{l}_i$ is the angular momentum transfer. At this point, the calculation of the angular scattering kernel is still fully quantum mechanical, although it is in the semiclassical limit. The extension to the classical limit of exchange of large numbers of rotational quanta is again similar to Eq. (3.21):

$$\left\langle \mathbf{l} \cdot \boldsymbol{\Theta}(0, 0) \mathbf{l} \cdot \boldsymbol{\Theta}(\theta_z, t) \right\rangle \big/ \hbar^2 = 2W_R(\mathbf{l}_f, \mathbf{l}_i) - \frac{i}{\hbar} t \Delta E_0^R - \frac{t^2}{\hbar^2} \Delta E_0^R k_B T_S - \frac{\Delta E_0^R k_B T_S \theta_z^2}{2\hbar^2 \omega_R^2}, \tag{3.26}$$

where $\Delta E_0^R = l_x^2/2I_{xx}^c + l_y^2/2I_{yy}^c + l_z^2/2I_{zz}^c$ is the rotational recoil energy, the $I_{xx,yy,zz}^c$ are the principal moments of inertia of a surface molecule and ω_R is a weighted average

of libration frequencies of the surface molecules in the z-direction. The constant ω_R plays a similar role for rotational transfers as the weighted average of parallel phonon velocities v_R in Eq. (3.22). Both of these quantities can be computed if the complete dynamical structure function of the surface is known although they are usually treated as parameters. The principal moments I^c_{ii} are normally expected to be those of a surface molecule in the case of a molecular target. However, if the projectile molecules are large and strike more than one surface molecule simultaneously, then I^c_{ii} is expected to become an effective moment of inertia, larger than that of a single molecule. In the case of monatomic solids, an effective surface molecule consisting of two or more surface atoms must be chosen. In either case, the product $\omega_R^2 I^c_{ii}$ can be regarded as an alternative choice of the parameter ω_R.

The result of combining the rotational kernel of Eq. (3.26) with the phonon kernel of Eq. (3.17) is a transition rate for the scattering of a rigid rotator molecule given by

$$\begin{aligned} w(\mathbf{p}_f, \mathbf{l}_f; \mathbf{p}_i, \mathbf{l}_i) = {} & \frac{\hbar^2}{S_{u.c}} |\tau_{fi}|^2 \left(\frac{(2\pi)^3 v_R^4 \omega_R^2}{(\Delta E_0^T)^2 \Delta E_0^R (k_B T_S)^3} \right)^{\frac{1}{2}} \\ & \times \left[\frac{\pi}{k_B T_S (\Delta E_0^T + \Delta E_0^R)} \right]^{\frac{1}{2}} \exp\left(- \frac{2\mathbf{P}^2 v_R^2}{4 k_B T_S \Delta E_0^T} \right) \\ & \times \exp\left(- \frac{2 l_z^2 \omega_R^2}{4 k_B T_S \Delta E_0^R} \right) \\ & \times \exp\left\{ - \frac{(E_f^T - E_i^T + E_f^R - E_i^R + \Delta E_0^T + \Delta E_0^R)^2}{4 k_B T_S (\Delta E_0^T + \Delta E_0^R)} \right\}. \end{aligned} \tag{3.27}$$

This result is similar to the atomic scattering expression of Eq. (3.22) but with additional terms contributed by the rotational degrees of freedom. In particular, the Gaussian-like term in energy transfer includes the difference between final and initial rotational energies as well as the rotational recoil, and there is an additional Gaussian-like expression in the surface-normal component of the rotational angular momentum. Additional prefactors have also appeared.

3.4.4. Molecular internal vibration modes

The remaining task is to include in the transition rate the contributions from vibrational excitations of the internal modes of the molecular projectile. If these modes are treated in the harmonic limit, and consistently with the semiclassical approximations used in obtaining the translational and rotational scattering kernels, the problem becomes that of a collection of forced harmonic oscillators (Mahan, 1990). The general result has been worked out for the case of surface scattering (Manson, 1988), and the internal mode scattering kernel can be written in the following form:

$$K_V(t, T_B) = \sum_{\kappa,\kappa'=1}^{N_A} e^{i(\mathbf{p}_f \cdot \Delta \mathbf{r}^f_{\kappa,\kappa'} - \mathbf{p}_i \cdot \Delta \mathbf{r}^i_{\kappa,\kappa'})/\hbar} e^{-W^p_{V,\kappa}(\mathbf{p}_f, \mathbf{p}_i)} e^{-W^p_{V,\kappa'}(\mathbf{p}_f, \mathbf{p}_i)} e^{Q^p_{V,\kappa,\kappa'}(\mathbf{p}_f, \mathbf{p}_i, t)}, \tag{3.28}$$

where N_A is the number of atoms in the molecule. The position of the κth atom of the molecule just before the collision (i) or just after (f), is given by expressions of the form $\mathbf{r}_\kappa^i(t) = \mathbf{r}_\kappa^i + \mathbf{u}_\kappa^i(t)$ so that, for example, $\Delta\mathbf{r}_{\kappa,\kappa'}^f = \mathbf{r}_\kappa^f - \mathbf{r}_{\kappa'}^f$. The vibrational displacement $\mathbf{u}_\kappa^i(t)$ relative to $\mathbf{r}_\kappa^i$ due to the internal mode, decomposed into cartesian components denoted by β, is

$$u_\kappa^\beta(t) = \sum_{j=1}^{N_v} \sqrt{\frac{\hbar}{2N_v m_\kappa \omega_j}}\, e(_j^\kappa|\beta)[a_j e^{-i\omega_j t} + a_j^+ e^{i\omega_j t}], \tag{3.29}$$

where N_v is the total number of internal modes and m_κ is the mass of the κth molecular atom. a_j and a_j^+ are, respectively, the annihilation and creation operators for the jth mode of frequency ω_j, and $e(_j^\kappa|\beta)$ is the polarization vector which is obtained from a normal modes analysis of the molecule.

The displacement correlation function for internal vibration modes of the projectile molecule is then written as

$$\begin{aligned} Q_{V,\kappa,\kappa'}^p(\mathbf{p}_f, \mathbf{p}_i, t) = {} & \sum_{\alpha,\alpha'=1}^{3} p_\alpha p_{\alpha'} \sum_{j=1}^{N_v} \frac{1}{2N_v\hbar\sqrt{m_\kappa m_{\kappa'}}\omega_j} e(_j^\kappa|\alpha) e^*(_j^{\kappa'}|\alpha') \\ & \times \big\{ n_M(\omega_j) e^{i\omega_j t} + \big[n_M(\omega_j) + 1\big] e^{-i\omega_j t} \big\}, \end{aligned} \tag{3.30}$$

where $n_M(\omega_j)$ is the Bose–Einstein function for an assumed equilibrium distribution of initial molecular vibrational states. The Debye–Waller factor associated with the κth atom of the projectile molecule becomes

$$W_{V,\kappa}^p(\mathbf{p}_f, \mathbf{p}_i) = \frac{1}{2} Q_{V,\kappa=\kappa'}^p(\mathbf{p}_f, \mathbf{p}_i, t = 0). \tag{3.31}$$

In the internal mode correlation function $Q_{V,\kappa,\kappa'}^p(\mathbf{p}_f, \mathbf{p}_i, t)$ the normal modes commute with each other since they are independent, and Eq. (3.30) can be further expanded to (Wyld, 1993)

$$\begin{aligned} e^{Q_{V,\kappa,\kappa'}^p(\mathbf{p}_f,\mathbf{p}_i,t)} &= e^{\sum_{j=1}^{N_v} Q_{j_{V,\kappa,\kappa'}}^p(\mathbf{p}_f,\mathbf{p}_i,t)} \\ &= \prod_{j=1}^{N_v} \sum_{\alpha_j=-\infty}^{\infty} \left\{ I_{|\alpha_j|}\big(b_{\kappa,\kappa'}(\omega_j)\big) \left[\frac{n_M(\omega_j)+1}{n_M(\omega_j)}\right]^{\alpha_j/2} e^{-i\alpha_j\omega_j t} \right\}, \end{aligned} \tag{3.32}$$

where $I_{|\alpha_j|}(z)$ is the modified Bessel function of integer order α_j and argument z. The argument of the modified Bessel function of Eq. (3.32) is given by

$$\begin{aligned} b_{\kappa,\kappa'}(\omega_j) = {} & \sum_{\alpha,\alpha'=1}^{3} p_\alpha p_{\alpha'} \frac{1}{N_v\hbar\sqrt{m_\kappa m_{\kappa'}}\omega_j} e(_{\nu_j}^\kappa|\alpha) e^*(_{\nu_j}^{\kappa'}|\alpha') \\ & \times \sqrt{n_M(\omega_j)\big[n_M(\omega_j)+1\big]}. \end{aligned} \tag{3.33}$$

Equations (3.28) through (3.33) define the scattering kernel for excitation of internal molecular modes.

The three scattering kernels for translation, rotation and internal vibrations can now be inserted back into Eq. (3.15) and all integrals can be readily carried out. The general result for the transition rate is

$$
\begin{aligned}
&w(\mathbf{p}_f, \mathbf{l}_f, \mathbf{p}_i, \mathbf{l}_i) \\
&\quad = \frac{1}{\hbar^2}|\tau_{fi}|^2\left(\frac{2\pi\hbar^2 v_R^2}{\Delta E_0^T k_B T_S}\right)\left(\frac{2\pi\hbar^2\omega_R^2}{\Delta E_0^R k_B T_S}\right)^{1/2} \\
&\qquad \times \left(\frac{\pi\hbar^2}{(\Delta E_0^T + \Delta E_0^R)k_B T_S}\right)^{1/2} \exp\left[-\frac{2\mathbf{P}^2 v_R^2}{4\Delta E_0^T k_B T_S}\right]\exp\left[-\frac{2l_z^2\omega_R^2}{4\Delta E_0^R k_B T_S}\right] \\
&\qquad \times \sum_{\kappa,\kappa'=1}^{N_A}\left\{e^{i(\mathbf{p}_f\cdot\Delta\mathbf{r}^f_{\kappa,\kappa'} - \mathbf{p}_i\cdot\Delta\mathbf{r}^i_{\kappa,\kappa'})/\hbar} e^{-W^p_{V,\kappa}(\mathbf{p}_f,\mathbf{p}_i)} e^{-W^p_{V,\kappa'}(\mathbf{p}_f,\mathbf{p}_i)}\right. \\
&\qquad \times \prod_{j=1}^{N_v}\sum_{\alpha_j=-\infty}^{\infty} I_{|\alpha_j|}\big(b_{\kappa,\kappa'}(\omega_j)\big)\left[\frac{n_M(\omega_j)+1}{n_M(\omega_j)}\right]^{\alpha_j/2} \\
&\qquad \left.\times \exp\left[-\frac{(E_f^T - E_i^T + E_f^R - E_i^R + \Delta E_0^T + \Delta E_0^R + \hbar\sum_{s=1}^{N_v}\alpha_s\omega_s)^2}{4(\Delta E_0^T + \Delta E_0^R)k_B T_S}\right]\right\}.
\end{aligned}
\tag{3.34}
$$

The transition rate of Eq. (3.34) is actually expressed, for compactness, as a product over all normal modes labeled by j and a summation over the excitation quantum number denoted by α_j. To obtain the discrete transition rate to a particular internal mode final state or combination of states, one takes the corresponding (j, α_j)th term of Eq. (3.34).

The result of Eq. (3.34) retains many of the features of the simpler expressions of Eqs. (3.22) and (3.1) for atomic scattering with the exchange of only phonons. The dominant feature is the Gaussian-like function containing the three different modes of energy exchange (phonons, rotations and internal molecular vibrations) together with the recoil terms from phonons ΔE_0^T and from rotational exchange ΔE_0^R. The width of the Gaussian-like function varies as the square root of the temperature and the sum of the two recoil energies. This is not a true Gaussian because of the momentum dependencies of the recoil energies. There are also Gaussian-like functions in the exchange of parallel momentum $\mathbf{P}$ and perpendicular angular momentum l_z that arise from retaining the correct momentum conservation conditions for a smooth surface. The envelope factors vary as negative powers of the temperature multiplied by recoil energies. These envelope factors guarantee the overall unitarity of the total scattered intensity, i.e., as the temperature and/or incident energy is increased, the maximum intensity of the Gaussian-like function decreases in order that the total integral over final states remains constant.

In Eq. (3.34) the quantum behavior of the internal mode excitations is expressed differently than the classical behavior for translational and rotational motion. The strength of the α_j quantum excitation of the jth mode is proportional to the modified Bessel function $I_{|\alpha_j|}(b_{\kappa,\kappa'}(\omega_j))$. Because these are quantum features the vibrational contribution to the Debye–Waller factor is still present, as are quantum phase factors involving the positions $\mathbf{r}_\kappa$ of the individual molecular atoms before and after the collision. The presence of these quantum phase factors can cause interference effects, but because in an actual experiment

the orientation of a molecule is not measured, the transition rate must be averaged over molecular orientations in order to compare directly with experiments. Recoil effects due to the excitation of internal modes are not explicitly apparent in Eq. (3.34), but they are included within the modified Bessel function.

In many cases, such as where the incident molecular energy and the surface temperature are not large compared to the energy of internal molecular vibrational excitations, the expansion of Eq. (3.34) to only single quantum excitations is sufficient. This expansion is

$$
\begin{aligned}
&w(\mathbf{p}_f, \mathbf{l}_f, \mathbf{p}_i, \mathbf{l}_i) \\
&\quad = \frac{1}{\hbar^2}|\tau_{fi}|^2 \left(\frac{\pi\hbar^2}{(\Delta E_0^T + \Delta E_0^R)k_B T_S}\right)^{1/2} \left(\frac{2\pi\hbar^2 v_R^2}{\Delta E_0^T k_B T_S}\right) \\
&\qquad \times \left(\frac{2\pi\hbar^2\omega_R^2}{\Delta E_0^R k_B T_S}\right)^{1/2} \exp\left[-\frac{2\mathbf{P}^2 v_R^2}{4\Delta E_0^T k_B T_S}\right] \exp\left[-\frac{2l_z^2\omega_R^2}{4\Delta E_0^R k_B T_S}\right] \\
&\qquad \times \sum_{\kappa,\kappa'=1}^{N_A} e^{i(\mathbf{p}_f\cdot\Delta\mathbf{r}^f_{\kappa,\kappa'} - \mathbf{p}_i\cdot\Delta\mathbf{r}^i_{\kappa,\kappa'})/\hbar} e^{-W^p_{V,\kappa}(\mathbf{p}_f,\mathbf{p}_i)} e^{-W^p_{V,\kappa'}(\mathbf{p}_f,\mathbf{p}_i)} \\
&\qquad \times \left\{ \exp\left[-\frac{(E_f^T - E_i^T + E_f^R - E_i^R + \Delta E_0^T + \Delta E_0^R)^2}{4(\Delta E_0^T + \Delta E_0^R)k_B T_S}\right] \right. \\
&\qquad + \sum_{\gamma,\gamma'=1}^{3} p_\gamma p_{\gamma'} \sum_{j=1}^{N_v} \frac{1}{2\hbar N_v \sqrt{m_\kappa m_{\kappa'}}\omega_j} e(^{\kappa}_{j}|\gamma) e^*(^{\kappa'}_{j}|\gamma') \\
&\qquad \times \left(n_M(\omega_j) \exp\left[-\frac{(E_f^T - E_i^T + E_f^R - E_i^R + \Delta E_0^T + \Delta E_0^R - \hbar\omega_j)^2}{4(\Delta E_0^T + \Delta E_0^R)k_B T_S}\right] \right. \\
&\qquad + \big(n_M(\omega_j) + 1\big) \\
&\qquad \left.\left. \times \exp\left[-\frac{(E_f^T - E_i^T + E_f^R - E_i^R + \Delta E_0^T + \Delta E_0^R + \hbar\omega_j)^2}{4(\Delta E_0^T + \Delta E_0^R)k_B T_S}\right] \right) \right\}. \qquad (3.35)
\end{aligned}
$$

Of the three terms in Eq. (3.35) the one proportional to $n_M(\omega_j)+1$ gives the single quantum creation rate, the term proportional to $n_M(\omega_j)$ is for single quantum annihilation, and the third term is the rate for scattering with no internal mode excitation.

3.4.5. Interaction potential

In obtaining the molecular scattering transition rates of Eqs. (3.34) and (3.35) the major input so far has been the statistical mechanics and the general conservation laws governing the various degrees of freedom. The interaction potential determines the scattering form factor $|\tau_{fi}|^2$. In the semiclassical limit of interest here τ_{fi} has been identified as the transition matrix for inelastic scattering, calculated from the elastic part of the potential, i.e., the transition rate for the elastic potential extended off of the energy shell (Manson et al., 1994). A very useful expression is one suggested by Mott and Jackson in their very early work, and is the same as is used for most applications of the distorted wave Born approximation. This is to let τ_{fi} be the off-energy-shell matrix element of the elastic part of the

molecule–surface potential taken with respect to its own eigenfunctions between the initial and final state. An example of this is the Mott–Jackson matrix element of an exponentially repulsive potential

$$V^0(z) = V_0 e^{-\beta z}. \tag{3.36}$$

This is a one-dimensional potential, and its matrix elements are given by (Goodman and Wachman, 1976)

$$v_{J-M}(p_{fz}, p_{iz}) = \frac{\hbar^2\beta^2}{m} \frac{\pi q_i q_f (q_f^2 - q_i^2)}{\cosh(\pi q_f) - \cosh(\pi q_i)} \left(\frac{\sinh(\pi q_f)\sinh(\pi q_i)}{q_i q_f} \right)^{1/2}, \tag{3.37}$$

where $q_i = p_{iz}/\hbar\beta$ and $q_f = p_{fz}/\hbar\beta$.

In the semiclassical limit of a hard repulsive surface, $\beta \to \infty$, the Jackson–Mott matrix element, as well as matrix elements for other 1-D potentials with a hard repulsive part, becomes

$$v_{J-M}(p_{fz}, p_{iz}) \to 2p_{fz}p_{iz}/m. \tag{3.38}$$

Since this is a quite general limiting case for a large class of potentials having a strong repulsive term to represent the surface barrier it is reasonable to use it as an approximation for τ_{fi}. In the comparisons of calculations with experimental data discussed in the sections below, this is the form factor that is applied.

The Van der Waals force between the surface and the incident molecular projectile gives rise to an attractive well in front of the surface. This is the physisorption well and it can have important effects at low incident translational energies. In the case of classical scattering, the main consequence of the Van der Waals attractive potential is to enhance the energy of the incoming particle associated with the direction normal to the surface. This is a refractive effect quite similar to that which occurs for light waves in optical media. Since refraction is the dominant effect, the potential can be modeled by a one-dimensional potential well and for a given well depth $|D|$, the refraction does not depend on the functional shape of the attractive part of the potential. Thus, this attractive force can be simulated by an attractive one-dimensional square-well potential in front of the repulsive barrier, and the width of the well is unimportant. The effect of the collision process is to replace the perpendicular component of the momentum p_{qz} near the surface and inside the well by a larger value p'_{qz}, which includes the depth D

$$p'^2_{qz} = p^2_{qz} + 2m|D|. \tag{3.39}$$

This refracts all projectiles at the leading edge of the well and causes them to collide with the repulsive barrier with a higher normal energy. The expressions for projectile translational energy and for scattering angle inside of the potential well become, respectively

$$E'^T_{f,i} = E^T_{f,i} + |D|, \tag{3.40}$$

and

$$\cos(\theta'_f) = \left(\frac{E^T_f \cos^2(\theta_f) + |D|}{E^T_f + |D|} \right)^{1/2}. \tag{3.41}$$

Transition rates calculated for molecular scattering inside the well can then be projected to the asymptotic region outside the well by multiplication with an appropriate Jacobian function, which can be easily determined from Eqs. (3.40) and (3.41).

3.5. Comparisons with experiment

In the following a number of comparisons of calculations with experimental data are presented for several different types of experiments that illustrate the importance of multiphonon energy transfer in molecule–surface collisions. There are four different categories of experiments considered, (1) angular distributions for which the measured quantity is the total scattered intensity regardless of energy or internal state, (2) translational energy resolved spectra taken at fixed incident and detector angles, usually measured by time-of-flight methods, (3) rotational energy resolved spectra, and (4) probabilities for excitation of internal molecular vibrational modes.

3.5.1. Angular distributions

There is a long history of measurements of angular distributions in atomic and molecular scattering from surfaces and two recent examples are shown here, O_2 scattering from Al(111) and CH_4 scattering from Pt(111). The O_2/Al(111) system is interesting because of recent work that has exhibited an anomaly in the adsorption probability associated with the incident beam angle. Although it is well-known that aluminum oxidizes readily, the Al(111) surface is surprisingly resistant to oxide formation upon bombardment with oxygen molecules. Recent molecular beams scattering experiments provide evidence for the existence of a weakly bound molecular state, one whose binding energy is less than 0.1 eV (Weiße et al., 2003). An extremely interesting feature observed in this work was a clearly pronounced dip in the observed backscattered O_2 intensity in the neighborhood of incident beam angles of 25° with respect to the surface normal, and at energies in the range between 90 and 300 meV. This feature is interesting because the authors of Ref. (Österlund et al., 1997) found an enhancement of the sticking probability at nearly the same incident conditions, raising the intriguing question of why should the sticking probability be substantially larger, not at normal incidence as expected, but at an incident polar angle where the normal translational momentum is significantly reduced. The observed increase in sticking associated with a concomitant decrease in scattering intensity occurring over a narrow angular range implies a very specific mechanism may be responsible. Molecular dynamics simulations utilizing a potential energy surface containing three molecular degrees of freedom support the proposition that this feature is caused by steering into a shallow molecular adsorption well located above the same position in the surface unit cell as the maximum in the barrier towards dissociative adsorption (Weiße et al., 2003). Conventional spectroscopic measurements such as HREELS and UPS have not observed molecular O_2 in a precursor state. However, the steering mechanism of Ref. (Weiße et al., 2003) provides an explanation for the absence of observable adsorbed O_2 because such a state would have a lifetime too short to be measurable by conventional spectroscopy.

Early STM experiments indicated that exposing Al(111) to a room temperature gas of O_2 led to isolated adsorbate atoms at very low coverage, while at coverages above 3% 1×1 islands of oxygen were formed (Brune et al., 1993). More recently Österlund et al. (1997) showed, in a molecular beams study, that the chemisorption reaction probability was below 1% for O_2 beams of very low translational energy, at or just above 25 meV, but rapidly rises to 90% as the incident energy is increased to 1 eV. They interpreted the reaction as direct dissociative desorption. A series of experiments using X-ray photoelectron spectroscopy (XPS) and high resolution electron energy loss spectroscopy (HREELS) were interpreted as indicating that the dissociative desorption is precursor mediated (Zhukov et al., 1999). Very recent molecular beams experiments, corroborated by STM measurements and supported by theoretical molecular dynamics simulations, gave evidence for the existence of an abstraction channel in the dissociative adsorption (Komrowski et al., 2001; Binetti et al., 2003). On the other hand, independent STM studies have pointed out that there are alternative interpretations of the observed oxygen adsorption features (Schmid et al., 2001). Thus, the picture emerging from these widely differing experimental investigations is that the oxidation of Al(111) is a complicated process, probably consisting of several simultaneous and overlapping channels. Clearly, it is of interest to examine the available scattering data for the O_2/Al(111) system in order to investigate the role that energy exchange to the phonon field of the surface may be playing and how such energy exchange may affect the sticking process.

Examples of the experimentally measured O_2 scattering angular distributions from clean Al(111) are shown in Figs. 3.1 and 3.2 and compared to the theoretical calculations using Eq. (3.27). The calculations are averaged over an incident beam with a Maxwell–Boltzmann distribution of rotational energies with rotational temperature 35 K. The solid curves are calculations for a potential with well depth $D = 50$ meV and the dash-dotted curves are for $D = 0$. There are two parameters in the theoretical expression of Eq. (3.27), the weighted parallel phonon speed v_R and frequency ω_R. For v_R we have chosen the value 2300 m/s for calculations used to fit the data shown in this paper. In general, v_R is expected to be of the order or somewhat smaller than the Rayleigh velocity (Brako and Newns, 1982; Brako, 1982), so the value chosen here compares favorably with the Rayleigh speed measured at 3200 m/s for the ⟨110⟩ and ⟨112⟩ symmetry directions of Al(111) (Lock et al., 1988). The value of ω_R is taken to be 10^{10} s^{-1}, but the calculated results are essentially independent of ω_R for values of this small order of magnitude.

In Fig. 3.1 it is seen that the theory predicts broad angular distributions with FWHMs of about 20° and peak maxima located near the specular positions or slightly subspecular, in reasonable agreement with experiment. The effect of including a well in the interaction is to shift the calculated angular distribution slightly in the supraspecular direction. This shift can be understood on the basis of the larger average energy losses caused by the molecule colliding with the repulsive surface at a higher effective energy and a more normal collision angle inside the well. Overall, the calculations shown in Fig. 3.1 with a 50 meV well seem to agree somewhat better with the experiment than those without a well, although such a statement cannot be made unambiguously because the agreement also depends on the choice of v_R. Nevertheless, the agreement shown in Fig. 3.1 indicates that the results are not inconsistent with the presence of a small attractive well such as proposed in Weiße et al. (2003).

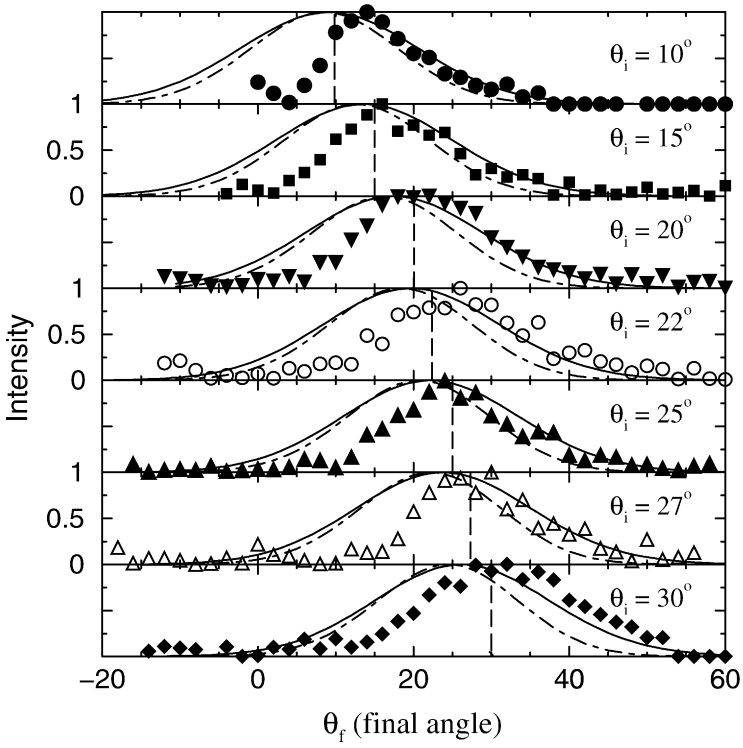

Fig. 3.1. Angular distributions of O_2 scattering from Al(111) for different incident angles as shown with an incident energy $E_i = 90$ meV and surface temperature $T_S = 298$ K. The experimental data points are shown as symbols (Ambaye et al., 2004). The calculated results are shown as solid curves for a potential with well depth $D = 50$ meV, and as dash-dotted curves for $D = 0$.

It is noticeable in Fig. 3.1 that the experimental points appear to lie below the calculated curves at final angles in the neighborhood of the normal direction, and this is especially the case when the incident angle is also near normal. This disagreement may be an artifact of correcting the scattered intensity for the small fraction of the incident beam that can enter the detector from the rear, before striking the surface, when the detector and incident beam directions are close to each other. In the case of incident angles smaller than 20° an over-compensation of the correction for this effect may account for much of the apparent discrepancy between experiment and theory (Ambaye et al., 2004).

Figure 3.2 shows the most interesting behavior of the measured scattering data. For $E_i = 90$ meV and a fixed incident angle $\theta_i = 20°$ the temperature dependent evolution of the angular distribution lobes is exhibited for $98 < T_S < 300$ K. At the lowest temperatures the most probable intensity occurs at an angle of about 25°, slightly larger than specular. However, as the temperature is increased up to room temperature the angular distribution lobe undergoes a shift towards the normal direction and even becomes slightly subspecular. Near specular or subspecular angular distribution lobes are not expected on the basis of predictions from simple theoretical models that do not allow for parallel momentum

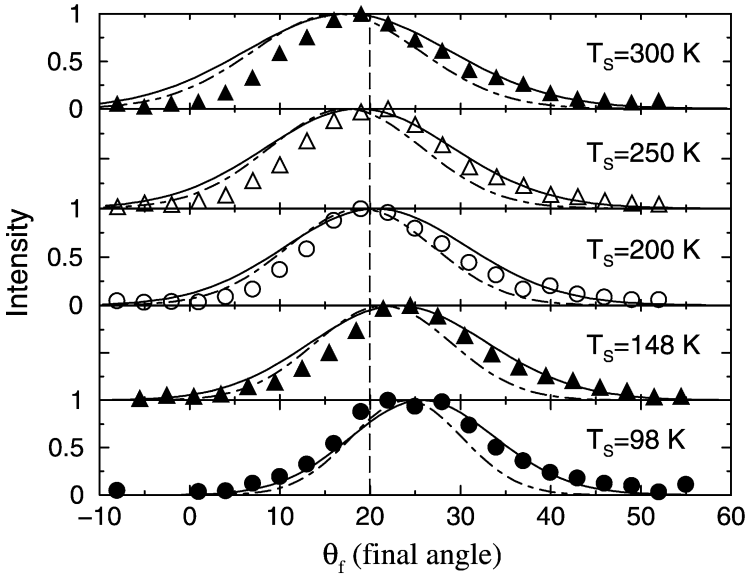

Fig. 3.2. Angular distributions for O_2/Al(111) as a function of surface temperature. The incident angle and energy are $\theta_i = 20°$ and $E_i = 90$ meV. The data are shown as symbols (Ambaye et al., 2004), and the calculated curves are for $D = 50$ meV (solid curve) and $D = 0$ (dash-dotted curve) as in Fig. 3.1.

exchange with the surface. In situations where the incident energy is large compared to the surface temperature the molecule will lose a significant fraction of its incident translational energy. Thus, if the parallel momentum of the projectile is not allowed to change, the perpendicular momentum will become much smaller which would predict a distinctly supraspecular angular distribution lobe.

However, the current theoretical models of Eq. (3.34) allows for the correct transfer of momentum parallel to the surface, i.e., the parallel momentum of the scattered particle is equal to the parallel momentum of the incident particle plus whatever parallel momentum is gained or lost to the phonons exchanged. Perpendicular momentum, on the other hand, is not conserved due to the broken symmetry presented by the surface. Perpendicular momentum is indeed exchanged with the surface, but there is no conservation law in that direction. Thus, the projectile's final perpendicular momentum is determined by the combined laws of energy conservation and parallel momentum conservation.

Clearly, the agreement between theory and experiment shown in Fig. 3.2 indicates that the temperature dependence of the angular distribution data can be explained by a theory containing the correct conservation laws, i.e., the present theory explains the subspecular shift with increasing temperature. As the temperature is increased, proportionately less energy is lost on average by the scattered particles (i.e., they are heated up). Because of the constraint of conservation of parallel momentum, more of this increase in energy goes into the increase of final normal momentum, thus making the angular distribution shift towards the normal.

As a second example of angular distributions, recently available data for the scattering of methane from clean and ordered Pt(111) (Yagu et al., 1999, 2000, 2001; Tomii et al., 2000; Kondo et al., 2002a, 2003a; Kondo, private communication) are presented and compared with calculations (Moroz and Manson, 2005). The experimental apparatus is constrained to a fixed angle of 90° between the beam incident at the angle θ_i and the final detector direction θ_f, thus for the measured angular distributions each final angle corresponds to a different incident angle according to the relation $\theta_f = 90° - \theta_i$. The energy resolution of the incident beam was $\Delta E/E = 0.06$ and the angular dispersion was less than 0.5° (Yagu et al., 2000).

Pt(111) is highly reactive and over a period of time under bombardment by the CH_4 beam the surface becomes contaminated with adsorbed molecules as well as dissociation products. In the experiment careful studies were made to assess the rate of build-up of contaminant products on the surface (Kondo et al., 2002a) and it was found that for initial periods of several minutes after routine cleaning protocols were completed the surface remained clean and the quality of the scattered spectra did not degrade. Thus all measurements considered are for scattering from a clean and uncontaminated surface.

For the calculations the incident molecular beam is chosen to be in a state that approximates an equilibrium distribution of rotational and vibrational states at low temperatures. The incident beam is averaged over a Boltzmann distribution of rotational states at a temperature of 30 K, approximately the estimated experimental conditions. The vibrational temperature is estimated to be significantly less than 100 K and for the calculations presented here a value of 10 K was used. The calculations are essentially unchanged by variations of more than a factor of two in either of these parameters. The calculated results are averaged over angular orientation of the molecules, and over angular orientation of the angular momentum. The detector used in these experiments is a velocity-dependent density detector, and consequently the calculated spectra must be corrected by a factor of $1/p_f$ in order to compare with the measurements.

The calculations require the polarization vectors for the normal modes of the CH_4 molecule. These were obtained using a standard classical normal modes analysis in the harmonic approximation (Wilson et al., 1955; Nakamoto, 1970; Woodward, 1972). For CH_4 there are a total of nine normal modes that have four distinct frequencies, three of which are degenerate. Calculations indicate that only the two lowest frequency modes with energies $\hbar\omega = 190.2$ and 161.9 meV are appreciably excited under the experimental conditions considered here, with the maximum excitation probability at $E_i = 500$ meV of approximately 4% and 5%, respectively.

Angular distributions for the CH_4/Pt(111) system were measured at two incident energies, $E_i = 190$ and 500 meV, and for surface temperatures ranging from 400 to somewhat over 800 K. The crystal azimuthal direction was $\langle 11\bar{2}\rangle$. Figure 3.3 shows the experimental data compared to calculations for an angular distribution taken at a temperature of 827 K. The calculated curve is obtained by integrating the differential reflection coefficient of Eq. (3.34) over all final energies and final angular momenta, averaging over an initial Boltzmann rotational distribution at a temperature of 30 K, summing over all excitations of internal vibrational modes, and averaging over molecular orientations. The well depth is taken to be $D = 40$ meV and the crystal mass M_C is that of a single Pt atom.

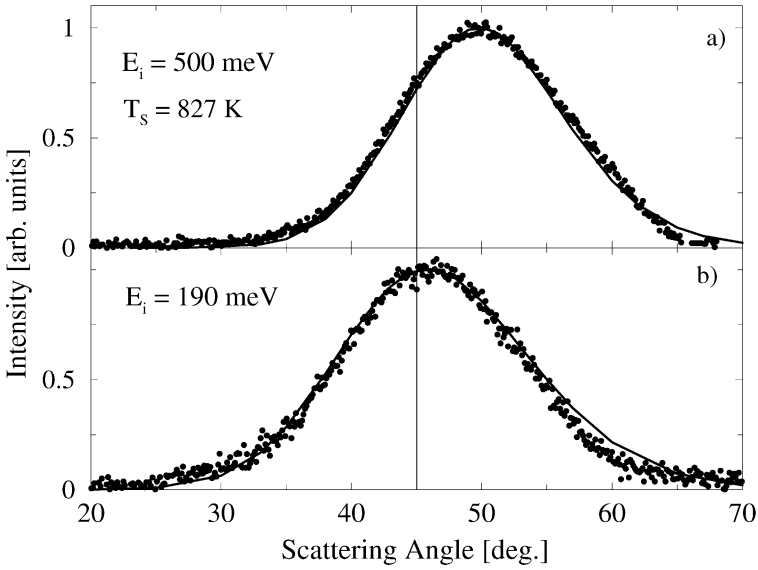

Fig. 3.3. Angular intensity distributions for methane CH_4 scattered from a Pt(111) surface compared to the calculations shown as solid curves. The incident translational energies are: (a) 500 meV; (b) 190 meV. The surface temperature is 827 K. Data is from Kondo et al., (2002b, 2003b). The vertical line marks the specular position.

It is seen that the most probable angle of the angular distributions are slightly supraspecular at the lower incident energy and approximately 5° larger than the specular position at the higher energy. The specular position $\theta_S = 45°$ is indicated by the vertical line. The experimental data and in particular the supraspecular shift with increasing energy are well described by the calculations. In addition the small decrease in full width at half maximum (FWHM) with the larger energy is matched by the calculations.

The temperature dependence of the angular distributions is shown in Fig. 3.4 which gives a series of graphs at the lower incident translational energy of 190 meV ranging from $T = 400$ to 700 K. Also shown is the data at $T = 827$ K from Fig. 3.3 which was taken on a different day. All other conditions are the same as in Fig. 3.3. It is seen that with increasing temperature there is a small subspecular shift of the most probable scattering angle towards the specular position and an increase in the full with at half maximum, both of which are well matched by the calculations. This subspecular shift is similar to the case for O_2/Al(111) discussed above in Fig. 3.2 and also was observed for methane scattering from LiF(001) (Moroz and Manson, 2004).

3.5.2. Translational energy resolved spectra

Multiphonon energy transfer is perhaps most clearly manifest in translational energy resolved spectra and this will be discussed using examples of time-of-flight measurements of methane scattering from both Pt(111) and LiF(001). The experimental measurements on scattering of CH_4 from a clean ordered LiF(001) surface that are considered here were taken by the same experimental group as the data for the angular distributions in Figs. 3.3

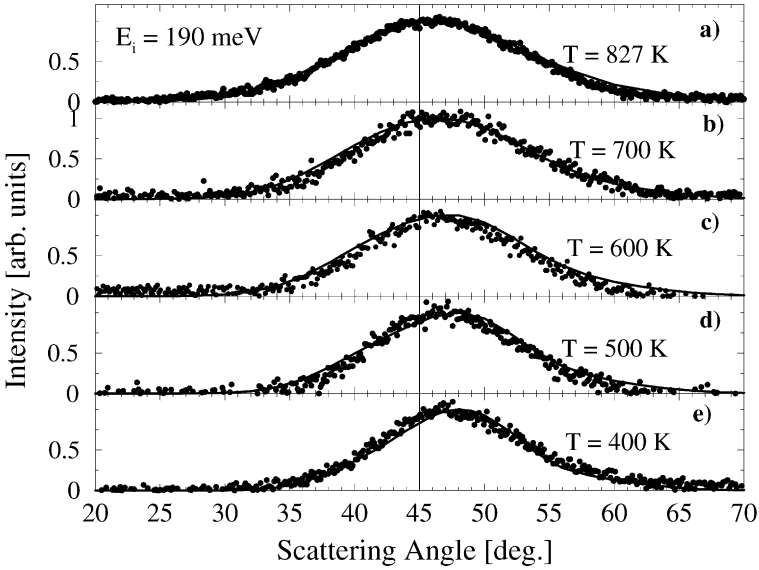

Fig. 3.4. CH_4/Pt(111): Angular intensity distributions for different surface temperatures T_S = 827 (a), 700 (b), 600 (c), 500 (d) and 400 K (e) as marked. The incident energy is 190 meV and the vertical line marks the specular position. Data is from Kondo et al. (2002b, 2003b).

and 3.4. They were carried out with an incident molecular beam whose translational energy varied between 190 and 500 meV by heating the supersonic jet nozzle and seeding with helium gas (Yagu et al., 2000). Surface temperatures were varied from 300 K to 700 K. All measurements were carried out in the scattering plane, which contains the incident beam and the surface normal. The detector was positioned at a fixed angle of 90° from the incident beam, meaning that the incident and final angles at which all measurements were taken are related by $\theta_f = 90° - \theta_i$.

An example of TOF energy-resolved spectra compared with calculations based on Eq. (3.34) is shown in Fig. 3.5. The experimental data are exhibited as points for the incident energy of 350 meV. The surface temperature is 300 K and the crystal azimuthal direction is ⟨110⟩. The incident angle goes from $\theta_i = 30°$ to $\theta_i = 50°$ implying final angles from 60° to 40° which gives a good sampling ranging across the maxima observed in the angular distributions which were also measured for this system. The vertical lines in each figure indicate the TOF time for elastic scattering (dashed line) and the time corresponding to the Baule estimate of recoil energy loss for hard sphere scattering at these angles (dashed-dotted line) assuming masses of methane and LiF. The Baule estimate is identical for all of the incident angles because the fixed-angle constraint between incident beam and detector makes the total scattering angle always the same.

The calculations from Eq. (3.34) shown as solid curves are the sum of the differential reflection coefficient over all final rotational angular momenta and all molecular internal modes, and are for a potential well depth of zero, a rotational temperature of the incident beam of 30 K, and an incident beam vibrational temperature of 10 K. The principal mo-

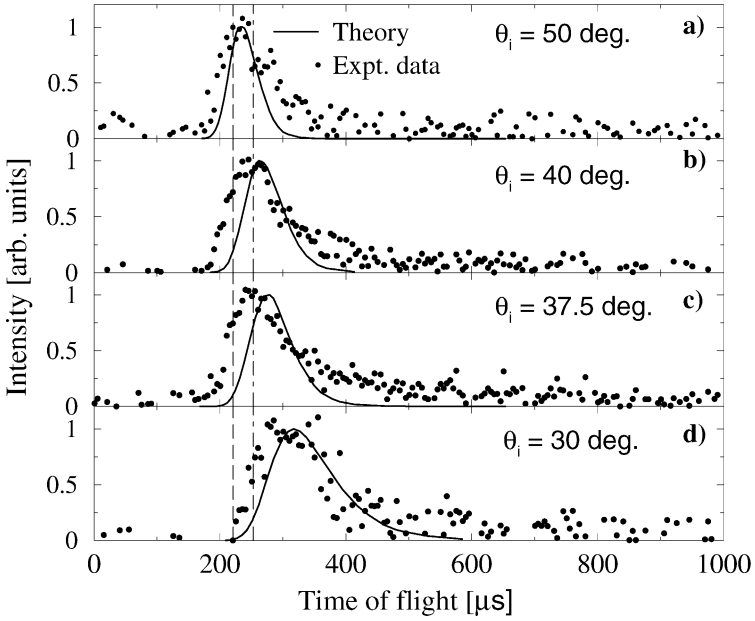

Fig. 3.5. Time of flight distributions of CH_4 molecules scattered from a LiF(001) surface in the ⟨110⟩ azimuthal direction for different incident angles $\theta_i = 50°$ (a); 40° (b); 37.5° (c) and 30° (d). The incident translational energy is 350 meV and the surface temperature is 300 K. The experimental measurements are shown as data points (Yagu et al., 2000; Tomii et al., 2000) and the calculations are shown as solid lines. The vertical dashed line is the position of elastic scattering and the vertical dash-dot line indicates the hard-sphere energy loss position.

ments of inertia of the CH_4 and LiF molecules were calculated classically with the known atomic masses and molecular bonding distances leading to values of the principal moments of inertia of $I_M = 5.26 \times 10^{-47}$ kg m^2 for CH_4 and $I_C = 3.41 \times 10^{-46}$ kg m^2 for LiF. The velocity v_R was chosen to be 1500 m/s which provides a reasonable fit to all data for both TOF spectra and angular distributions. Interestingly, decreasing v_R by a factor of two has very little effect on the position of the maximum in the calculated TOF distribution but it increases the width by about 10%, particularly on the large time side. Conversely, increasing v_R by a factor of two narrows the distribution by about 10% but again leaves the maximum in nearly the same position. The corresponding weighted rotational speed parameter ω_R was chosen to be 10^{10} s^{-1} but for values of this small magnitude the calculated results are completely independent of ω_R. For the value of M_C, the effective mass of the surface molecules, we have used three times the mass of an LiF molecule. A larger effective mass indicates a collective effect in which the incident projectile is colliding with more than a single LiF molecule. The initial analysis using the washboard model carried out by the authors of the experimental study also required surfaces masses several times larger than that of a single LiF (Yagu et al., 2000).

The angular dependence of the energy resolved measurements is clearly shown in Fig. 3.5. It is interesting to note that the translational energy losses are greater for a beam with near-normal incidence than for one with more grazing incidence. For $\theta_i = 30°$ (and

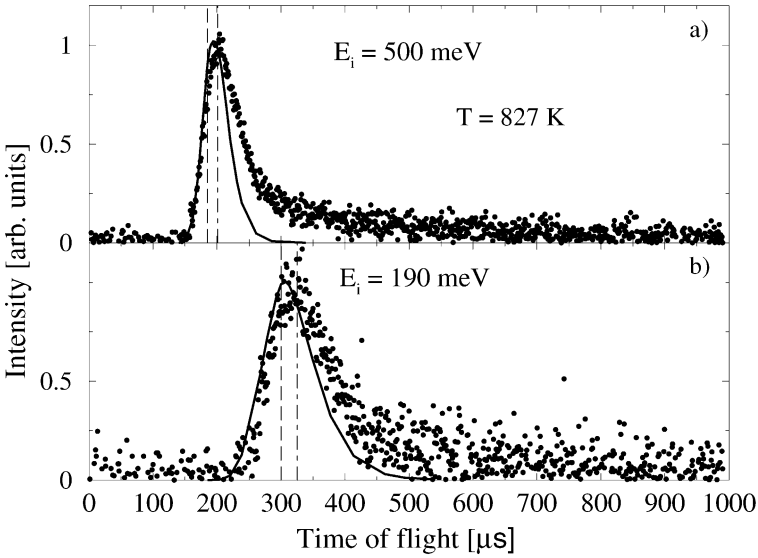

Fig. 3.6. Time of flight spectra of CH_4 molecules scattered from a Pt(111) surface for different translational energies: 500 meV (a) and 190 meV (b). The incident angle is $\theta_i = 45°$ and the surface temperature is 827 K. The two vertical lines indicate the Baule recoil energy loss (dashed-dotted line) and elastic scattering (dashed line) as in Fig. 3.5. The data is from Kondo et al. (2002b, 2003b).

$\theta_f = 60°$) very few molecules gain energy from the surface and emerge with final energies larger than the incident energy. However, for the more grazing incident beam having $\theta_i = 50°$ (and $\theta_f = 40°$) a significant fraction of the molecules actually gain translational energy from the surface. The calculations follow nicely the incident angular trends observed in the experimental data. Both the data and calculations illustrate the limitations of the simple Baule estimate for the energy loss. For near-normal incident beams the average final energy is substantially less than the Baule estimate, while for more grazing angular incidence the average energy is larger than the Baule estimate.

An example of translational energy-resolved spectra for methane scattering from the Pt(111) surface is shown in Fig. 3.6 for $E_i^T = 190$ and 500 meV and a surface temperature of 827 K. The incident beam and detector angles are both 45°. The calculations shown as solid curves are with a well depth of $D = 40$ meV. As in Fig. 3.5 the TOF time corresponding to elastic scattering is indicated by the vertical dashed line and the Baule estimate for energy transfer is indicated by the dash-dotted vertical line which at this specular scattering angle is about 15% of the incident energy. It is seen that under these scattering conditions the measured most probable final energy shows an energy loss of approximately the same as the expected recoil loss with a single surface atom, but there is a significant fraction of scattered CH_4 molecules that leave the surface at energies larger than that of the incident beam. The FWHM of the scattered distribution becomes significantly smaller with increasing incident energy. The calculated curves match the peak position and the high energy (small TOF time) of the data, but again as in the case of CH_4/LiF(001) of Fig. 3.5 they do not explain the long tail at low energies.

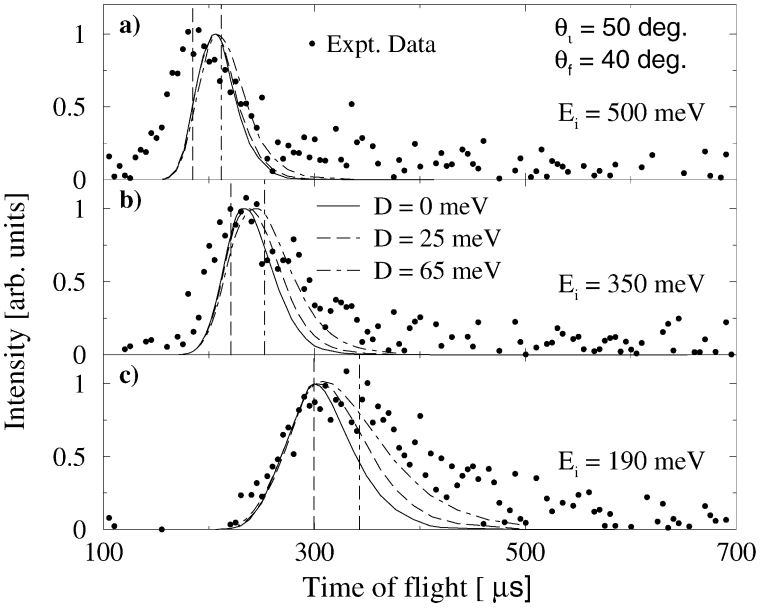

Fig. 3.7. CH_4/LiF(001): Time of flight distributions for different values of well depth $|D|$. The incident energies are: 500 meV (a); 350 meV (b); 190 meV (c). The incident angle is $\theta_i = 50°$ and the surface temperature is 300 K. The experimental measurements are shown as data points (Yagu et al., 2000; Tomii et al., 2000; Kondo et al., 2002a) and the calculations for $D = 0$, 25 and 65 meV shown as solid, long-dashed and dot-dashed lines, respectively. The vertical lines indicate elastic and hard sphere scattering as in Fig. 3.5.

The next example shows one way in which important physical information about the interaction potential can be obtained from the translational energy resolved spectra, in this case information about the physisorption well. Figure 3.7 shows the TOF data for CH_4/LiF(001) at the three incident energies of 190, 350 and 500 meV for $\theta_i = 50°$ compared with calculations with well depths $D = 0$, 25 and 65 meV. At lower incident energies, for the TOF measurements better agreement between data and theory are obtained when an attractive well is included in the potential. At the highest incident energy of 500 meV the presence of a well, which in this case is significantly smaller than the energy, has little effect on the calculated results. However, at the lowest energy of 190 meV there is a significant effect. At all incident energies, the effect of the well is not significant at small TOF times, but it increases the calculated intensity at large TOF times (small final energies) and gives a small shift of the most probable final energy towards smaller final energies. Both of these latter effects bring the calculations into better agreement with experiment, with the best agreement corresponding to the larger well. The comparisons between experiment and calculations in Fig. 3.7 indicate that not only does the physisorption well strongly influence the multiphonon energy transfer at lower incident energies, but also in some cases can be used to estimate the well depth.

3.5.3. Rotational energy resolved spectra

A number of experimental studies have made direct measurements of the exchange of translational energy to rotational energy (Mortensen et al., 2003; Sitz et al., 1988; Janda et al., 1983; Budde et al., 1987), usually presented as plots of the scattered average translational energy $\langle E_f^T \rangle$ as a function of rotational energy E_f^R. These plots generally show a negative correlation, that is to say the average translational energy tends to decrease with increasing rotational energy. Intuitively, such behavior would be suggested by the law of conservation of energy as applied to these two degrees of freedom, but this is not completely valid because there is always the possibility of energy transfer to and from the surface and the internal vibrational modes.

Discussed here is one of these experiments for NO scattering from Ag(111) (Rettner et al., 1991). A series of graphs of $\langle E_f^T \rangle$ versus E_f^R is shown in Fig. 3.8. The surface temperature is 450 K, incident translational energies range from 99 meV to 963 meV, and the measurements were made under specular conditions with incident angles ranging from 15° to 60° as marked. In all cases except for the lowest energy incident beam, the average final energy decreases by 10–20% over the range of measured final rotational energies,

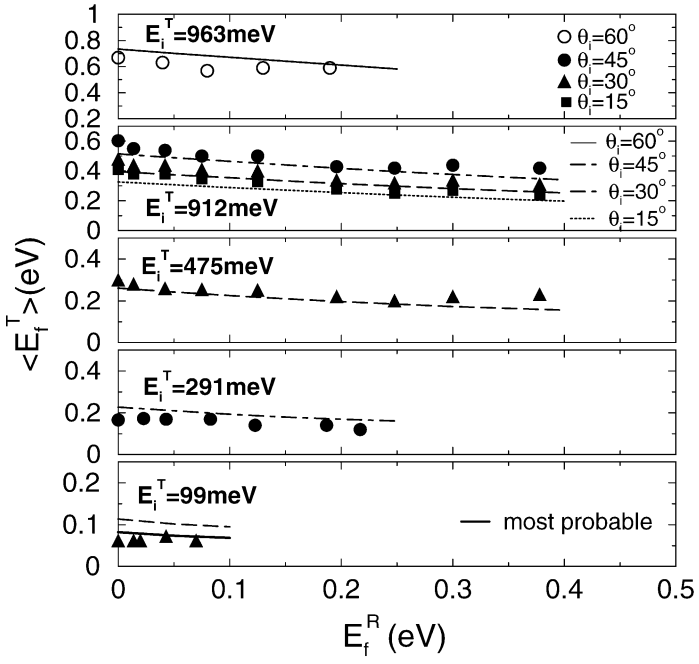

Fig. 3.8. NO/Ag(111): Final average translational energy as a function of final rotational energy for several incident energies and angles taken at the specular scattering angle. In each panel the experiment and theory for a given incident energy and angle are compared. Open circles are data at $\theta_i = 60°$, solid circles are data at 45°, solid triangles are data at 30° and solid squares are data at 15°. Calculations are the curves in each panel. $T_S = 450$ K. The solid curve in the panel for $E_i^T = 99$ meV is the calculated most probable final translational energy. Data are taken from Rettner et al. (1991).

which in some cases extends to as large as 400 meV. Our calculations, shown as curves, also reproduce this same behavior rather well except for the lowest energy.

The case of the low energy $E_i^T = 99$ meV beam requires further examination. As opposed to the higher energy measurements, there is essentially no decrease in measured average final energy as E_f^R increases and the final energy is about 60% of the incident energy. This would indicate that a large fraction of the incident translational energy is transferred to the surface lattice and relatively little is being converted to molecular rotational energy. The theoretical calculations, on the other hand, predict a 10% decrease over the measured E_f^R energy range, and additionally they predict that the average final translational energy should be larger than the incident energy rather than smaller as measured.

The answer to both of these discrepancies appears to lie in the manner in which the average final translational energy is defined. It appears to be customary to report experimental measurements as average final translational energies but, however, what is actually measured is closer to the most probable final energy corresponding to the peak position in the intensity versus final translational energy (Luntz, private communication; Sitz, private communication). For large incident beam energies, there is usually little discrepancy between the two definitions but this is not necessarily the case for low energy beams. At low energies comparable to the surface temperature there can be a significant fraction of the scattered particles that gain energy from the surface and this causes the energy-resolved spectra to become quite skewed and non-symmetric about the most probable final energy. Thus the average and most probable energies can become quite different, whereas for high energy incident beams they usually are nearly the same.

The solid curve shown in the lower panel of Fig. 3.8 for $E_i^T = 99$ meV is the most probable final translational energy as a function of E_f^R. This appears at a position of net energy loss and shows less dependence on E_f^R in much better agreement with the experimental points. Thus it appears that, with this reinterpretation of the experimental points at low incident beam energy, the theory predicts relatively well the exchange of energy between translational and rotational degrees of freedom of the molecule, in addition to predicting the overall energy loss or gain to the surface phonon field.

A second type of experiment involving rotational energy resolution consists of measurements of the scattered intensity as a function of final rotational energy. Several examples of such spectra for the scattering of NO by Ag(111) are shown in Fig. 3.9 in which the scattered intensity with the detector in the scattering plane and positioned at the specular angle ($\theta_f = \theta_i$) is plotted as a function of final rotational energy in a semi-logarithmic graph (Rettner et al., 1991; Kleyn et al., 1981). In Fig. 3.9(a) the surface temperature for all measurements was 650 K, the upper three sets of data were measured at an angle $\theta_i = 15°$ with three different incident translational energies (Kleyn et al., 1981), 1000 meV (open circles), 750 meV (filled circles) and 320 meV (open diamonds); the fourth data set (filled diamonds) was taken for $E_i^T = 320$ meV and $\theta_i = 40°$. Figure 3.9(b) shows a second set of measurements for the same system taken by the same group at a later date. All those measurements were for $\theta_i = 15°$ and two different energies and temperatures: $E_i^T = 850$ meV and $T_S = 273$ K (open squares), $E_i^T = 850$ meV and $T_S = 520$ K (filled squares), and $E_i^T = 90$ meV and $T_S = 520$ K (open triangles) (Rettner et al., 1991). The intensities are presented in arbitrary units, and for clarity the various data sets are separated by arbitrary constant amounts.

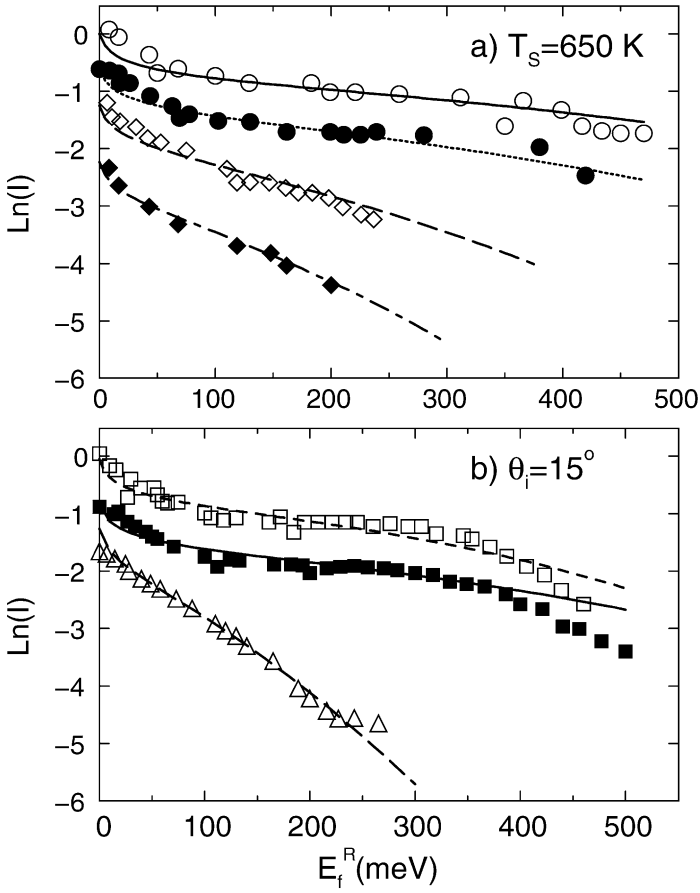

Fig. 3.9. NO/Ag(111): Final rotational energy resolved intensity at specular scattering angles for several incident energies and surface temperatures. (a) Data taken from Kleyn et al. (1981): $T_S = 650$ K; open circles are data for $E_i = 1000$ meV and $\theta_i = 15°$, solid circles are data $E_i = 750$ meV and $\theta_i = 15°$, open diamonds are data for $E_i = 320$ meV and $\theta_i = 15°$ and solid diamond is data $E_i = 320$ meV and $\theta_i = 40°$. (b) Data taken from Rettner et al. (1991). $\theta_i = 15°$; open squares are data for $E_i = 850$ meV and $T_S = 273$ K, solid squares are data for $E_i = 850$ meV and $T_S = 520$ K and triangles are data for $E_i = 90$ meV and $T_S = 520$ K. Curves are calculations.

These experimental measurements exhibit several evident characteristics; the intensity decreases strongly with increasing rotational energy and there is a steep initial decrease for small E_f^R followed by a large range of E_f^R for which the intensity decreases nearly exponentially (i.e., nearly a straight line in the logarithmic plot). For some of the measurements, in particular for those taken at higher incident beam energies, there is a second pronounced decrease in intensity for very large E_f^R. This high rotational energy feature is termed the rotational rainbow and its onset marks the classical limit of angular momentum transfer to a molecule in a single scattering collision.

Also shown in Fig. 3.9 are curves calculated from Eq. (3.34). For each final rotational energy these calculations are the sum of the differential reflection coefficient over the internal vibrational stretch mode excitations, final translational energies, and an average is carried out over all possible molecular orientations. The differential reflection coefficient is also averaged over an assumed Maxwell–Boltzmann distribution of initial rotational states with a temperature $T_R = 35$ K which is in approximate agreement with experimental conditions (Kleyn et al., 1981). A distribution of incident molecular vibrational frequencies at a temperature of 125 K, somewhat larger than the rotational temperature, is also assumed in agreement with estimated experimental conditions. The calculations were found to depend only weakly on the distribution of initial rotational states as long as the average rotational energy was small compared to the incident translational energy, and this is discussed further in connection with Fig. 3.11 below. The velocity parameter v_R is given a value of 1000 m/s and ω_R is taken to be 10^{10} s^{-1}, but as in previous cases the results are not strongly dependent on these parameters, and in this case are not affected even by changes of a factor of two or more.

Relatively good quantitative agreement is seen between calculations and experiment. The initial steep decline in intensity is somewhat overemphasized by the calculations but it occurs over the same energy range as the observations. The long plateau of exponential decay for intermediate energies is well matched. The calculations do not reproduce the rotational rainbow behavior observed at higher incident energies, but this is understandable because the simple interaction potential of Eq. (3.38) used to calculate the scattering form factor does not include the possibility of a rainbow.

The data of Fig. 3.9(a) have in an earlier study been analyzed using molecular dynamics simulations that included a relatively sophisticated interaction potential energy surface (Kimman et al., 1986). This study obtained a good description of the experimental data and in particular obtained a correct prediction of the rotational rainbow. The same molecular dynamics study was used to explain the data for final translational energy as a function of rotational energy shown above in Fig. 3.8 (Muhlhausen et al., 1985). The present work demonstrates that most of the observed features, with the exception of the rotational rainbow, are not strongly dependent on details of the potential energy landscape but instead arise largely from the statistical mechanics of the scattering process.

A more recent and quite extensive experimental examination of a different system, N_2 scattering from Cu(110), is shown in the rotational energy spectra of Fig. 3.10. These measurements cover a range of incident beam translational energies from 90 to 1000 meV, surface temperatures from 100 to 700 K as marked and the measurements were made for incident and final angles nearly normal to the surface (Siders and Sitz, 1994). Each of these sets of experimental points is compared to calculations carried out with similar incident beam parameters as in the previous graphs. In this case the calculated curves agree quantitatively with the measurement for the whole rotational energy range except in some cases for the highest energy points measured. The experimental points at small E_f^R values for most incident conditions display the rather sharp decrease exhibited in the calculations, but at large E_f^R there is little indication of rotational rainbow cut-off behavior.

One interesting point that arises from the comparisons of calculations with the rotational energy spectra data is that for nearly all incident conditions reported, the calculations show a very sharp decrease at small rotational energy, and this decrease is observed in much of

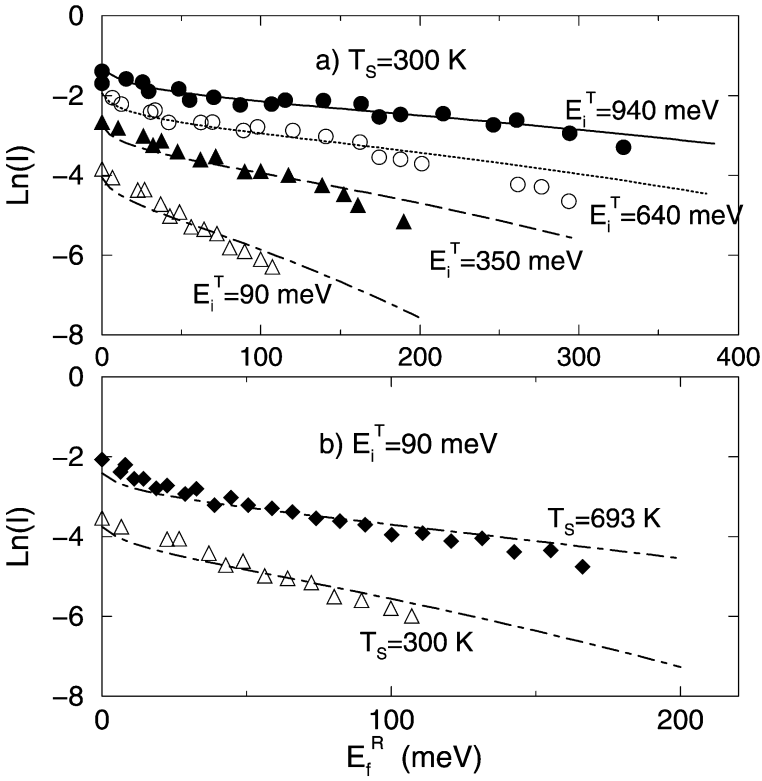

Fig. 3.10. The final rotational energy distribution under specular geometry conditions for several incident energies and surface temperatures for N_2/Cu (110). (a) $T_S = 300$ K; $E_i = 90$ meV, 350 meV, 640 meV and 940 meV as marked. (b) $E_i = 90$ meV; $T_S = 300$ K and $T_S = 693$ K. Symbols are experimental data from Siders and Sitz (1994) and curves are theory.

the available data. However, this data was obtained using molecular jet beams and these are known to produce very cold rotational distributions, typically of a few tens of K and relatively independent of translational energy. Our calculations indicate that the low E_f^R energy behavior is due to the cold incident rotational distribution and that if an incident beam with a rotational energy distribution comparable to the translational energy were used the effect would disappear. This is demonstrated in Fig. 3.11 which shows several calculations compared to the N_2/Cu(110) data for $E_i^T = 640$ meV and $T_S = 300$ K from Fig. 3.10. The dotted curve is the same calculation shown in Fig. 3.10 for an incident beam with a rotational temperature of 35 K. The dashed curve shows a calculation, not for a Boltzmann distribution of rotations, but for a beam with a single rotational energy of 13.4 meV for all N_2 molecules. This energy would correspond approximately to the $J = 7$ rotational quantum level. It is clear that the sharp decrease at low rotational energy is somewhat damped but the behavior at large E_f^R is essentially unchanged.

The solid curve in Fig. 3.11 is for an incident beam having a fixed rotational energy of 26.4 meV (approximately the same as the $J = 10$ rotational state) and it is seen that

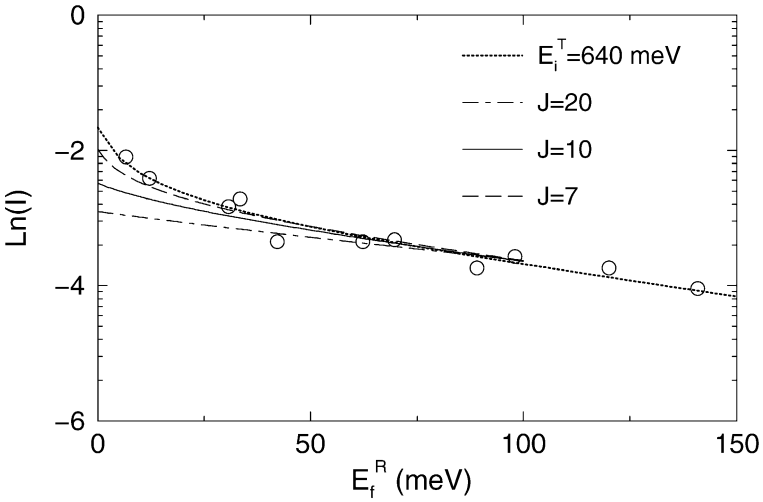

Fig. 3.11. The final rotational energy distribution for E_i = 640 meV and surface temperature 300 K for N_2/Cu(110). Symbols are experimental data from Siders and Sitz (1994), the dash curve is theory with a cold initial rotational distribution of $T_R = 35$ K, the long dash curve is theory with initial rotational state with $E_i^R = 13.4$ meV ($J = 7$), solid curve is theory with initial rotational state at 26.4 meV ($J = 10$) and dot dashed curve is theory with initial rotational state at 100.8 meV ($J = 20$). $\theta_i = \theta_f = 0°$.

the low energy decrease is significantly reduced. For the dash-dotted curve, the rotational energy is fixed at 100.8 meV, about the same as for the $J = 20$ quantum level, and the calculated rotational energy spectrum becomes nearly exponential over the entire energy range. However, all curves regardless of initial rotational state saturate to nearly the same behavior at large E_f^R. Thus, it appears clear that the anomalous behavior of the rotational energy spectra at small E_f^R is due to the cold rotational distribution of the incident beam. Although we did not show in Fig. 3.11 calculations that average over incident Boltzmann rotational distributions with very high temperatures, our calculations show that the effect is similar and that for high incident rotational temperatures the effect tends to disappear. This, in fact, could become a very useful effect. It indicates that careful measurements of the small E_f^R behavior of the spectra, when compared with calculations such as those presented here, can be used to determine the rotational energy distribution of the incident beam.

3.5.4. Internal vibrational mode excitation

Calculations for the excitation probability of the NO molecular stretch mode in collisions with an Ag(111) surface are presented here. At the incident energies involved in the present experiments the N–O stretch mode, which in the gas phase has a value of 233 meV, is only weakly excited. However, shown in Fig. 3.12 for the case of NO/Ag(111) is a comparison of calculation and experiment (Rettner et al., 1985) of the excitation probability for the first excited state of this mode as a function of incident translational energy. As for the previous calculations, a rotational temperature of 35 K is assumed for the incident beam,

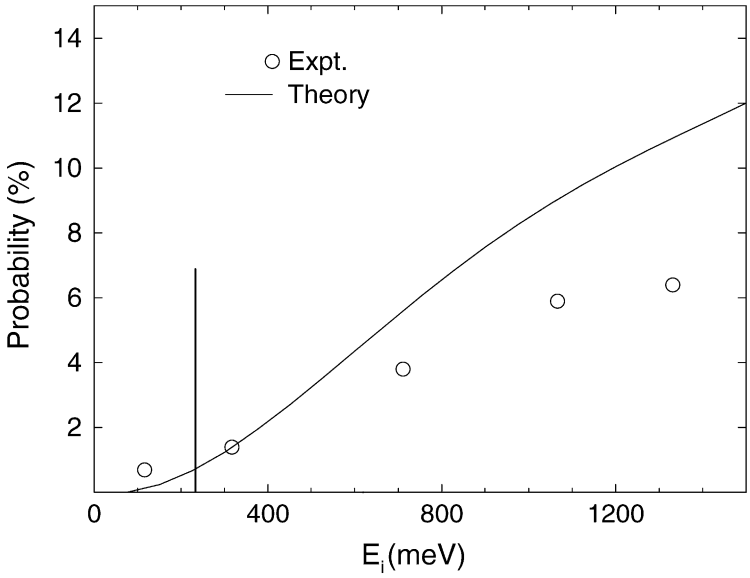

Fig. 3.12. NO/Ag(111): Probability for excitation of a single quantum of the internal stretch mode of the NO molecule as a function of incident energy compared with measured values (Rettner et al., 1985) shown as open circles. The vertical line indicates the gas-phase stretch mode energy of 233 meV. The surface temperature is 760 K and $\theta_i = \theta_f = 15°$.

and the incident and final angles are $\theta_i = 15°$ and $\theta_f = 15°$. The surface temperature is 760 K. The results have been averaged over all collisional orientations of the molecule and over angular directions of the angular momentum. It is seen that the internal mode excitation probability does not become appreciable until the incident translational energy is well above the mode excitation energy. However, due to coupling with the phonons, the energy supplied by the surface vibrations gives a small but non-zero probability of excitation even for incident translational plus rotational energy less than the threshold energy for internal mode excitation of NO. This is seen in both experiment and theory in Fig. 3.12. Excitation probabilities of 7–8% are predicted by the theory for incident translational energies of up to 1 eV. An alternative theoretical model, which calculates the excitation probability assuming that the forced harmonic oscillator behavior is due to electron–hole pair creation has been proposed by Newns (1986), and produces excitation probabilities which also agree well with the data of Fig. 3.12.

3.6. Conclusions

In experiments involving the collisions of molecular particles with a surface a major contributor to energy exchange is the excitation of phonon modes of the target. At the quantum level, which implies annihilation or creation of single phonons, observation of such processes can provide fundamental physical information on the dynamics of the surface and on the molecule–surface interaction potential. When multiple quanta of phonons are

excited a reduced amount of detail can be obtained about the surface dynamics, but multiphonon transfer needs to be understood because it presents a background that must be subtracted, or otherwise accounted for, in order to reveal features in the scattering spectra due to other mechanisms. In the classical limit of large kinetic energies, heavy molecular masses and high temperatures the multiphonon energy transfers become classical in nature, but even in that limit the multiphonon scattering spectra can reveal important information about the gas–surface collision process.

Presented in this paper is a brief review of theoretical descriptions of molecular beam scattering from surfaces. The theory is sufficiently rigorous that it reduces to an exact result for the simple problem of atomic elastic diffraction from surfaces, which involves only the three spatial degrees of freedom. Then, in a straight-forward manner, and initially with atomic projectiles, the theory is first developed to include single-phonon excitations, next to include excitations of a few phonons, and then it is extended to the classical limit of many-phonon transfers.

The results obtained for atomic projectiles are then extended to molecular particles within the decoupling approximation. Expressions are first developed for the scattering including classical rotational excitation of a rigid molecule. Finally, the internal molecular vibrational modes are included via a semiclassical quantum mechanical theory. At each of these levels it is possible to obtain expressions for the scattering transition rate that are written as closed-form analytic equations. In the multiphonon limit the transition rates are mixed quantum-classical in form. They are essentially classical in the projectile's translational and rotational degrees of freedom while quantum mechanical in the excitation of internal molecular vibrational modes.

The theory presents a clear and straight-forward picture of the multiphonon excitation and how it affects the dynamics of the other degrees of freedom involved in the molecular collision process. Although one important need for understanding multiphonon effects is for background subtraction in order to clearly reveal the features observed in the data caused by the other degrees of freedom, it is shown that measurements of the multiphonon spectra can reveal important physical information. Among these are the determination of the physisorption well depth, sensitivity to collective effects in the target through determination of effective masses, it can reveal the smoothness of the surface and produce mean-square corrugation amplitudes, it can provide information about the distribution of rotational energies in the incident molecular beam, energy transfer and accommodation coefficients can be measured, and it provides a beautiful example of the transition from the purely quantum mechanical regime of elastic and single-phonon scattering to the classical regime of multiquantum excitation.

A number of experimental measurements are analyzed in order to exhibit examples of the influence of multiphonon excitation on molecular scattering from surfaces. The first of these is a description of the angular distribution lobes observed when a molecular beam strikes the surface and the only measured quantity is the total number of particles scattered as a function of final angles. For molecules substantially heavier than hydrogen, the shapes of these lobes are well predicted as functions of the experimentally controllable parameters such as surface temperature, incident kinetic energy, incident angle, molecule species and surface composition.

A second type of scattering experiment involves making translational energy-resolved measurements at fixed angles. Classical multiphonon theory is shown in several examples to explain the measured properties of the energy transfer.

A third class of molecular scattering experiments are measurements of scattered intensity and final average translational energy as functions of rotational energy. Again, for the case of molecules that are larger than hydrogen, classical theories in the translational and rotational degrees of freedom appear to give a good description of the observed results.

The final example considered here is the excitation of internal molecular vibrational modes. This provides a good example of how multiphonon effects can be incorporated into a calculation primarily intended to explain the consequences of a different mechanism activated during the scattering process.

The approach described here has the advantage that, at least for single collision events, it can be expressed in terms of closed-form mathematical expressions, as opposed to other more numerically intensive methods such as molecular dynamics simulations or trajectory calculations. The analytic form of the results also means that this method of describing multiphonon transfers can readily be incorporated into scattering theories for other excitation processes, at least within the decoupling approximation. This is readily accomplished by expressing the scattering theory for the desired process as a time-dependent Fourier transform, and then convoluting with the multiphonon kernel as is done in Eq. (3.34). An example of this convolution process is the influence of multiphonon energy transfers on internal molecular vibrational mode excitation as discussed above in Section 3.5.4 in connection with Fig. 3.12. If, in the calculations, multiphonon transfers are ignored the internal mode excitation probabilities are substantially overestimated. The addition of multiphonon degrees of freedom, and the concomitant reduced amount of incident energy available because of energy loss to the surface modes, reduces the calculated probabilities and brings them into much better agreement with measurement. It also shows that phonon excitations can cause the appearance of non-zero internal mode excitation probabilities at incident translational energies well below the threshold at which the incident kinetic energy equals the mode energy.

The comparisons between theory and experiment exhibited here show that many of the features introduced into molecule–surface scattering spectra as a result of multiphonon excitation can be qualitatively, and often quantitatively, explained within the framework of a mixed quantum-classical theoretical treatment.

Acknowledgement

This work was supported by the National Science Foundation under grant number 0089503 and the U.S. Department of Energy under grant number DE-FG02-98ER45704.

References

Ambaye, H., Manson, J.R., Weiße, O., Wesenberg, C., Binetti, M., Hasselbrink, E., 2004. J. Chem. Phys. 121, 1901.

Armand, G., Manson, J.R., 1984. Phys. Rev. Lett. 53, 1112.
Armand, G., Manson, J.R., Jayanthi, C.S., 1986. Phys. Rev. B 34, 6627.
Barker, J.A., Auerbach, D.J., 1984. Surf. Sci. Rep. 4, 1.
Baule, B., 1914. Ann. Physik 44, 145.
Benedek, G., Toennies, J.P., 1994. Surf. Sci. 299, 587.
Binetti, M., Weiße, O., Hasselbrink, E., Katz, G., Kosloff, R., Zeiri, Y., 2003. Chem. Phys. Lett. 373, 366.
Bortolani, V., Levi, A.C., 1986. Rivista del Nuovo Cimento 9, 1.
Brako, R., 1982. Surf. Sci. 123, 439.
Brako, R., Newns, D.M., 1982. Phys. Rev. Lett. 48, 1859.
Brune, H., Wintterlin, J., Trost, J., Ertl, G., Wiechers, J., Behm, R.J., 1993. J. Chem. Phys. 99, 2128.
Brusdeylins, G., Doak, R.B., Toennies, J.P., 1980. Phys. Rev. Lett. 44, 1417.
Brusdeylins, G., Doak, R.B., Toennies, J.P., 1981. Phys. Rev. Lett. 46, 437.
Budde, F., Mödl, A., Hamza, A.V., Ferm, P.M., Ertl, G., 1987. Surf. Sci. 192, 507.
Burke, K., Gumhalter, B., Langreth, D.C., 1993. Phys. Rev. B 47, 12852.
Burke, K., Jensen, J.H., Kohn, W., 1991. Surf. Sci. 241, 211.
Campargue, R. (Ed.), 2001. Dynamics of Gas–Surface Interactions. Springer, Heidelberg.
Celli, V., 1984. In: Langreth, D., Suhl, H. (Eds.), Many Body Phenomena at Surfaces. Academic Press, New York, p. 315.
Celli, V., Himes, D., Tran, P., Toennies, J.P., Wll, Ch., Zhang, G., 1991. Phys. Rev. Lett. 66, 3160.
Dai, J., Manson, J.R., 2002. Nucl. Instrum. Methods Phys. B 193, 497.
Dai, J., Manson, J.R., 2003. J. Chem. Phys. 119, 9842.
For a discussion of the trajectory approximation with numerous references, see: DiRubio, C.A., Goodstein, D.M., Cooper, B.H., Burke, K., 1994. Phys. Rev. Lett. 73, 2768.
Estermann, I., Frisch, R., Stern, O., 1931. Z. Phys. 73, 348.
Estermann, I., Stern, O., 1930. Z. Phys. 61, 95.
Frisch, O.R., 1979. What Little I Remember. Cambridge University Press, Cambridge.
Goodman, F.O., 1974. Prog. Surf. Sci. 5, 261.
Goodman, F.O., Wachman, H.Y., 1976. Dynamics of Gas–Surface Scattering. Academic Press, New York, p. 255.
Gumhalter, B., 2001. Phys. Rep. 351, 1.
Gumhalter, B., Burke, K., Langreth, D.C., 1994. Surf. Rev. Lett. 1, 133.
Gumhalter, B., Langreth, D.C., 1999. Phys. Rev. B 60, 2789.
Hofmann, F., Toennies, J.P., Manson, J.R., 1994. J. Chem. Phys. 101, 10155.
Hofmann, F., Toennies, J.P., Manson, J.R., 1997. J. Chem. Phys. 106, 1234.
Hulpke, E. (Ed.), 1992. Helium Atom Scattering from Surfaces. Springer Series in Surface Sciences, vol. 27. Springer, Berlin.
Jackson, J.M., 1932. Proc. Cambridge Phil. Soc. 28, 136.
Jackson, J.M., Mott, N.F., 1932. Proc. Roy. Soc. A 137, 703.
Janda, K.C., Hurst, J.E., Cowin, J.P., Wharton, L., Auerbach, D.J., 1983. Surf. Sci. 130, 395.
Kimman, J., Rettner, C.T., Auerbach, D.J., Barker, J.A., Tully, J.C., 1986. Phys. Rev. Lett. 57, 2053.
Kleyn, A.W., Luntz, A.C., Auerbach, D.J., 1981. Phys. Rev. Lett. 47, 1169.
Knauer, F., Stern, O., 1929. Z. Phys. 53, 766.
Komrowski, A.J., Sexton, J.Z., Kummel, A.C., Binetti, M., Weiße, O., Hasselbrink, E., 2001. Phys. Rev. Lett. 87, 246103.
Kondo, T., Private communication.
Kondo, T., Sasaki, T., Yamamoto, S., 2002a. J. Chem. Phys. 116, 7673.
Kondo, T., Sasaki, T., Yamamoto, S., 2002b. J. Chem. Phys. 116, 7673.
Kondo, T., Sasaki, T., Yamamoto, S., 2003a. J. Chem. Phys. 118, 760.
Kondo, T., Sasaki, T., Yamamoto, S., 2003b. J. Chem. Phys. 118, 760.
Lennard-Jones, J.E., Devonshire, A.F., 1936a. Nature 137, 1069.
Lennard-Jones, J.E., Devonshire, A.F., 1936b. Proc. Roy. Soc. (London) A 156, 6.
Lennard-Jones, J.E., Devonshire, A.F., 1936c. Proc. Roy. Soc. (London) A 156, 29.
Lennard-Jones, J.E., Devonshire, A.F., 1936d. Proc. Roy. Soc. (London) A 156, 37.
Lennard-Jones, J.E., Devonshire, A.F., 1937a. Proc. Roy. Soc. (London) A 158, 253.
Lennard-Jones, J.E., Devonshire, A.F., 1937b. Proc. Roy. Soc. (London) A 158, 269.

Lock, A., Toennies, J.P., Wöll, Ch., 1988. Phys. Rev. B 37, 7087.
Luntz, A.C., Private communication.
Mahan, G.D., 1990. Many-Particle Physics. Plenum Press, New York and London.
Manson, J.R., 1988. Phys. Rev. B 37, 6750.
Manson, J.R., 1991. Phys. Rev. B 43, 6924.
Manson, J.R., 1994. Comput. Phys. Commun. 80, 145.
Manson, J.R., 1998. Phys. Rev. B 58, 2253.
Manson, J.R., Celli, V., Himes, D., 1994. Phys. Rev. B 49, 2782.
Manson, J.R., Tompkins, J., 1977. Proceedings of the 10th International Symposium on Rarefied Gas Dynamics. Prog. Astronautics and Aeronautics 51, 603.
Maradudin, A.A., Montroll, E.W., Weiss, G.H., 1963. Theory of Lattice Dynamics in the Harmonic Approximation. Academic Press, New York.
Meyer, H.D., Levine, R.D., 1984. Chem. Phys. 85, 189.
Micha, D.A., 1981. J. Chem. Phys. 74, 2054.
Moroz, I., Manson, J.R., 2004. Phys. Rev. B 69, 205406.
Moroz, I., Manson, J.R., 2005. Phys. Rev. B 71, 113405.
Mortensen, H., Jensen, E., Diekhöner, L., Baurichter, A., Luntz, A.C., Perunin, V.V., 2003. J. Chem. Phys. 118, 11200.
Muhlhausen, C.W., Williams, L.R., Tully, J.C., 1985. J. Chem. Phys. 83, 2594.
Muis, A., Manson, J.R., 1996. Phys. Rev. B 54, 2205.
Muis, A., Manson, J.R., 1997. J. Chem. Phys. 107, 1655.
Nakamoto, K., 1970. Infrared Spectra of Inorganic and Coordination Compounds. John Wiley and Sons, Inc., New York.
Newns, D.W., 1986. Surf. Sci. 171, 600.
Österlund, L., Zorić, I., Kasemo, B., 1997. Phys. Rev. B 55, 15452.
Powers, J., Manson, J.R., Sosolik, C., Hampton, J., Lavery, A.C., Cooper, B.H., 2004. Phys. Rev. B 70, 115413.
Rettner, C.T., Ashfold, M.N.R. (Eds.), 1991. Dynamics of Gas–Surface Interactions. The Royal Society of Chemistry, Cambridge.
Rettner, C.T., Fabre, F., Kimman, J., Auerbach, D.J., 1985. Phys. Rev. Lett. 55, 1904.
Rettner, C.T., Kimman, J., Auerbach, D.J., 1991. J. Chem. Phys. 94, 734.
Roberts, J.K., 1930. Proc. Roy. Soc. (London) A 129, 146.
Rodberg, L.S., Thaler, R.M., 1967. Quantum Theory of Scattering. Academic Press, New York.
Schmid, M., Leonardelli, G., Tcheließnig, R., Biedermann, A., Varga, P., 2001. Surf. Sci. 478, L355.
Scoles, G. (Ed.), 1988. Atomic and Molecular Beam Methods. Oxford University Press, Oxford.
Siders, J.L.W., Sitz, G.O., 1994. J. Chem. Phys. 101, 6264.
Sitz, G.O., Private communication.
Sitz, G.O., Kummel, A.C., Zare, R.N., 1988. J. Chem. Phys. 89, 2558. 2572, 6947.
Sjölander, A., 1959. Ark. Fys. 14, 315.
Stern, O., 1920a. Z. Phys. 2, 49.
Stern, O., 1920b. Z. Phys. 3, 27.
Stern, O., 1926. Z. Phys. 39, 751.
Strachan, C., 1935. Proc. Roy. Soc. (London) Ser. A 150, 456.
Toennies, J.P., 1987. Physica Scripta T 19, 39.
Toennies, J.P., 1991. In: Kress, W., de Wette, F.W. (Eds.), Springer Series in Surface Sciences, vol. 21. Springer, Heidelberg, p. 111.
Tomii, T., Kondo, T., Hiraoka, T., Ikeuchi, T., Yagu, S., Yamamoto, S., 2000. J. Chem. Phys. 112, 9052.
Weiße, O., Wesenberg, C., Binetti, M., Hasselbrink, E., Corriol, C., Darling, G.R., Holloway, S., 2003. J. Chem. Phys. 118, 8010.
Wilson, E.B., Decius, J.C., Cross, P.C., 1955. Molecular Vibrations. The Theory of Infrared and Raman Vibrational Spectra. McGraw-Hill.
Woodward, L.A., 1972. Introduction to the Theory of Molecular Vibrations and Vibrational Spectroscopy. Oxford University Press, Oxford.
Wyld, H.W., 1993. Methods for Physics. Addison-Wesley, New York.

Yagu, S., Hiraoko, T., Kino, Y., Yamamoto, S., 2000. Appl. Surf. Sci. 165, 217.
Yagu, S., Kino, Y., Hiraoos, T., Sasaki, M., Yamamoto, S., 2001. Appl. Surf. Sci. 169–170, 122.
Yagu, S., Kino, Y., Ozeki, K., Yamamoto, S., 1999. Surf. Sci. 433–435, 779.
Zhukov, V., Popova, I., Yates, J.T. Jr., 1999. Surf. Sci. 441, 251.